

## **Reply to Reviewers – Smith, Rheinwalt, and Bookhagen**

### Reviewer #3:

*The paper by Smith et al. argues that, for a given airborne lidar dataset, there exists an optimal resolution which minimizes the impact of both gridding errors and any uncertainty in the DEM in the calculation of topographic metrics.*

*I think this paper should eventually be published but I have serious concerns about the analysis that I urge the authors to consider prior to publication.*

Thank you for your detailed comments, thorough review, and time spent with the manuscript and code. We have done our best to respond to each of the comments individually, and make appropriate changes to the MS.

### Specific Comments:

*1) I am concerned with how the authors created their DEMs. When I create a DEM of a mathematical function I sample the function at regularly spaced points. The resulting DEM is an incomplete representation of the surface but it is an accurate representation where the function is sampled. When I compute slope and aspect using DEMs created this way there are errors associated with discretization, but they are small and converge to zero as the pixel size becomes small. As such, I was surprised by magnitude and types of errors computed by Smith et al. for their synthetic cases.*

*When I looked more closely, I saw the reason for this discrepancy. If I am interpreting the code [https://github.com/UP-RS-ESP/TopoMetricUncertainty/blob/master/gaussian\\_hill\\_example.py](https://github.com/UP-RS-ESP/TopoMetricUncertainty/blob/master/gaussian_hill_example.py) correctly, Smith et al. have generated their DEMs of Gaussian hills by randomly sampling a Gaussian function and then computing the mean elevation of those random samples within each domain. None of this is explained in the manuscript in the section on synthetic data analysis. Since no information is given, I have no idea how many random samples were used to compute the mean value, or why the authors choose to use the mean value. When scientists grid data from a point cloud, they generally use Independent Distance Weighting (IDW) because this method weighs measurement points close to the sample location more heavily than points farther from the sample. The author's approach is not an interpolation of any kind – it treats measurements points far from the DEM grid point location ( $x_i$ ,  $y_j$ ) equal to those close to the grid point location. DEM values are supposed to represent the elevation at each point on the surface. DEMs are never supposed to represent the mean elevation within some square domain. Yet, that is how they have been created in this manuscript and I believe that much of the error that the authors are studying is due to the nonstandard way that they have created their DEMs. To address this issue, I urge the authors to explain how their DEMs are created and use IDW to create the DEMs from the point cloud. I would further urge the authors not to assume a random sample in their synthetic DEMs, since lidar data are not a random sample. Before this error is fixed it is difficult to even fully review the paper. However, I will do the best I can, recognizing that this can only be a preliminary review until the DEMs are properly computed.*

We believe that there has been a substantial misunderstanding of our methods here, and we would like to clarify that we do not randomly sample a Gaussian function for our

synthetic data analysis, but rather sample a mathematical function at evenly spaced points, as the reviewer suggested is best practice.

In our github code, we provide two forms of synthetic data, one which is representative of a point cloud, and one which is created natively on a grid using equal-spaced sampling as expected by the reviewer. The functions found here: <https://github.com/UP-RS-ESP/TopoMetricUncertainty/blob/master/surfaces.py> are used to create our synthetic data that are used in the first part of the MS. We do not create a point cloud and take a mean of randomly-sampled points, as the reviewer suggests, but rather calculate the mathematical value of the given exponential term in the Gaussian function at each sampled (x, y) coordinate. This is explained in the MS on page 4, line 10, although we agree that this could be made more clear by explaining our gridding procedure or linking to the specific code used to create the surfaces. The secondary set of code that the reviewer linked to is a toy example with synthetic lidar data, and is not used in the MS. During data analysis and manuscript preparation we explored the impact of randomly sampling points akin to a lidar dataset. We were especially interested in the impact of X-Y offsets (gridding data with an uncertainty in the X/Y location) and point clustering. We do not present these results in the manuscript (as they would extent the already long manuscript even more), but kept this part of the code on the github archive. We have updated the Github landing page to be more explicit as to what each piece of code does, and which are used in the MS.

Given that we simply sample our Gaussian function at each point on our grid in equal steps, we can also sample the slope and aspect of that function (see Equations 1, 2), which are well-known at each point of our grid for a differentiable function. We then use those 'perfect' samples of slope and aspect at each sample point to compare to the slope and aspect grids calculated on our 'perfect' elevation grid using various algorithms. When we compare the computed difference of our 4-neighbor method to the derived values of TE on the same ideal grid (compare MS Figure 3 and Supplemental Figure 2), the magnitudes and directions are the same. We thus conclude that our TE model accurately captures the magnitude of algorithm-induced error on the synthetic surface.

We also believe there was also a misunderstanding of our methods with concern to the generation of the DEMs from the lidar point cloud. To clarify, we have generated our lidar DEMs using a triangular irregular network (TIN) approach, which is also widely used in the lidar community and implemented by LASTools (e.g., Isenburg et al, 2006). This is an alternative method to the weighted mean provided by IDW techniques, and also results in reliable lidar DEMs. To supplement our analysis and address the concerns related to DEM generation, we have generated DEMs from the same source lidar data using several alternative techniques, including IDW with several different parameters (Table 1 of this reply, new Supplementary Table 1, and Supplementary Figures 13-21). The difference between these elevation models is very small (see Figure 1 of this Reply and Supplementary Figures 13-21). For detailed processing methodologies, we refer to our manual here: [https://github.com/BodoBookhagen/Lidar\\_PC\\_interpolation](https://github.com/BodoBookhagen/Lidar_PC_interpolation)

**Table S1.** Listing of interpolation schemes used to create DEMs for SCI. For a more in-depth discussion of each method, we refer to our github page: <https://github.com/UP-RS-ESP/TopoMetricUncertainty>.

Scheme Name	Software/Algorithm Basis	Figure
Triangular Irregular Network	blast2dem, LAStools, LAStools (2017)	
Triangular Irregular Network, Delauney Method	triangulation, GMT, Watson (1982)	Figure S13
Local Mean	blockmean, GMT, Wessel and Luis (2017)	Figure S14
Local Median	blockmedian, GMT, Wessel and Luis (2017)	Figure S15
Inverse Distance Weights, power=1, radius=grid size $\times \frac{\sqrt{2}}{2}$	gdal_grid, GDAL (gdal.org), Shepard (1968)	Figure S16
Inverse Distance Weights, power=1, radius=grid size $\times \sqrt{2}$	gdal_grid, GDAL (gdal.org), Shepard (1968)	Figure S17
Inverse Distance Weights, power=1, radius=grid size $\times 2\sqrt{2}$	gdal_grid, GDAL (gdal.org), Shepard (1968)	Figure S18
Inverse Distance Weights, power=2, radius=grid size $\times \frac{\sqrt{2}}{2}$	gdal_grid, GDAL (gdal.org), Shepard (1968)	Figure S19
Inverse Distance Weights, power=3, radius=grid size $\times \frac{\sqrt{2}}{2}$	gdal_grid, GDAL (gdal.org), Shepard (1968)	Figure S20
Inverse Distance Weights, power=2, radius=grid size $\times \frac{\sqrt{2}}{2}$	Points2Grid, pdal (pdal.io), Shepard (1968)	Figure S21

**Table 1 – List of lidar interpolation schemes used in the preparation of this manuscript.** We use the TIN method from LAStools as our primary data source, but have also examined DEMs created with each other method. We refer to Supplementary Figures 13-21 for detailed comparisons of Elevation, Slope, TE, and PEU for each DEM generation method. One figure is also presented below in Figure 1 of this reply.

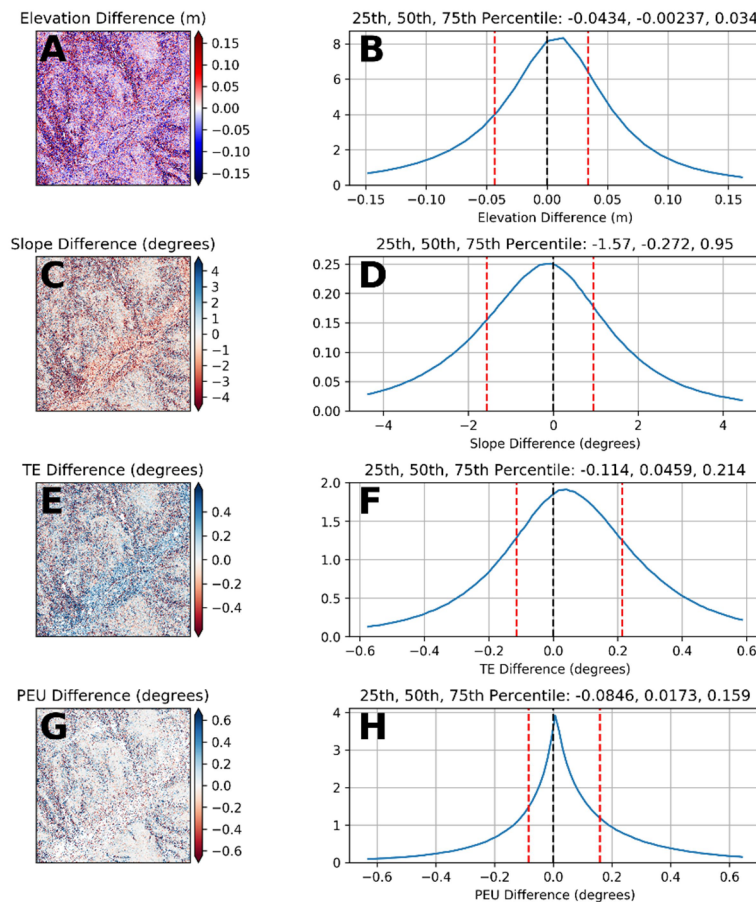


**Figure 1 – Impact of changed DEM interpolation method on a 1m DEM.** Left column shows difference for a zoomed in region of SCI for (A) elevation, (C) slope, (E) TE, and (G) PEU when a simple inverse distance weighting scheme is used as compared to the TIN method discussed in the MS. Color bar scaled from 5<sup>th</sup> to 95<sup>th</sup> percentiles. Right column shows the density histogram of the differences for the whole Pozo catchment. Red lines represent the 25<sup>th</sup> and 75<sup>th</sup> percentiles, with a black line centered on zero. Histograms scaled between 5<sup>th</sup> and 95<sup>th</sup> percentiles. While elevation differences are relatively small, they engender much larger slope errors. The difference in calculated TE and PEU between methods remains small.

Regardless of what gridding method is used, there will be some uncertainty in the derived elevation grid. This uncertainty is modified by the terrain type, accuracy of the lidar data, sampling scheme, and many other factors (as mentioned in the MS, page 12, Line 14). While we agree that we do not have a perfect error model – we assume that the standard deviation of the community of points in each lidar grid cell search radius is representative of the uncertainty in that lidar point elevation – we argue that the TE and PEU effects we see are independent of the error model used. We have experimented with different error models, including preferentially selecting more reliable points with lower scan angles (Rheinwalt and Bookhagen, 2018), but the spatial distribution of errors remains similar. Importantly, if a different error model exists, it can be directly included in our approach. Elevation uncertainty will be propagated into the slope and aspect calculations regardless of the DEM used, and the effect of DEM uncertainty on slope and aspect calculations will increase as the spacing of the DEM approaches the uncertainty magnitude.

*2) I am having difficulty understanding the error equations. In eqns 4 and 5 there is a partial derivative  $\partial_i$  with another partial derivative  $\partial_i / \partial_i$  as a subscript. I have never seen this syntax before. What does it mean? I am also confused by the reference to epsilons as uncertainties. In the paper, the epsilon values used to compute TE are computed using the standard deviations within each pixel, which is not the same as uncertainty. The uncertainty of a mean value can be quantified using a standard deviation, but only after being divided by the square root of the number of samples used to compute the mean. I am similarly confused by the use of standard deviations without any scaling by the number of samples in the PEU calculations.*

We have reviewed the equations here, and want to clarify our notation. We used a shorthand, which is more common in the physics community, to avoid writing double partial derivatives. We quantify the change in topographic metrics with a change of the topography – essentially  $dS / d(dz/dx)$ , which was not clearly stated. We have reformatted each of the equations in the updated MS to use the classic notation.

In reference to the second point, we think that the reviewer misunderstood our DEM generation method. As we mentioned above in the reply to the first comment, we use equally spaced samples ('gridding') of the mathematical function to create our elevation metrics, so we do not have any uncertainty or standard deviation to include in our TE calculation. We have explored these effects, but did not report them in the manuscript, as they require further analysis and are more appropriate for a subsequent paper.

The TE, as represented by Equations 4/5, does not involve the standard deviation, as it is based simply on the finite difference operation performed on the gridded dataset. The epsilon metric, defined in Equation 3, is an inherent error due to the second order finite difference approximation used here to calculate slope and aspect, and does not take into account any uncertainty in the elevation measurements. We only introduce a standard deviation in Equations 10/11, where the PEU is calculated independently of the TE.

We are unsure as to the reviewer's last point "*I am similarly confused by the use of standard deviations without any scaling by the number of samples in the PEU calculations*". The standard deviation is always calculated with knowledge of the number of samples – the formula for STD is the square root of the sum of squared differences from the mean divided by one minus the sample size. Perhaps this confusion is related



to the misunderstanding of our synthetic data creation methods. In any case, we calculate our PEU formulas by propagating the standard deviation of the elevation data into the directional derivatives used to calculate slope and aspect to arrive at a value for PEU.

*3) One of the metrics used by the authors, the truncation error is, according to the authors, “uncertainty associated with the representation of a continuous surface as a grid.” However, since landscapes have roughness at all scales (i.e., they are not differentiable and, more broadly, any increase in DEM resolution almost always results in additional real features being resolved in the topography), it is not necessarily the case that a polynomial is a better approximation of the surface than a straight line, as implied by the truncation error and the associated assumption that minimizing TE leads to a better result. I can see how TE would be a useful measure if topography was smooth at small scales, but I don’t think this is supported by observations of actual topography. To address this issue, the authors could explore and defend their choice of TE in landscapes with microtopography present (i.e., nearly all landscapes) or they could perform their analysis without using TE.*

Our metric of TE is technique based – when a three-point difference method is used to calculate a terrain derivative, there is always some error, excepting when the surface is perfectly flat. If we assume that additional features will always be resolved at higher resolutions, for example by modelling terrain as a fractal surface, slope is no longer defined, because the surface is not differentiable. In the case of our synthetic data (the Gaussian Hill), or with the gridded lidar data, we assume a differentiable surface, in which case slope is defined, and we can then calculate the magnitude of the TE for our finite-difference method. We can further test the magnitude of our TE on our synthetic surface, as described on page 7 of the MS, and check that the magnitude of TE from the finite-difference slope analysis matches the analytical solution for TE (compare Figures 3 and Supplemental Figure 2).

In our analysis, TE will always decrease with increasing spatial resolution – a finer grid will have less and less truncation error, whether or not the underlying surface is smooth or rough. However, depending on the application, one may not always want to minimize the TE (ie, to choose only the finest available spatial resolution) as PEU has an increasing effect at very fine scales. At the scale of microtopography, the uncertainty in the elevation data is often as large as the microtopography being resolved – for example, a DEM with a vertical accuracy of 10cm (the accuracy of a very good airborne lidar dataset) can resolve 10cm high features, but cannot decide if those features are signal or noise. The effect is even more pronounced when that DEM is then used to calculate slope or aspect (see Figure 1 of this Reply, where small elevation differences lead to large slope differences). At the fine scale, the PEU for slope and aspect grows very quickly, independent of the shrinking TE. As such, we argue that there exists a scale where the two independent errors and uncertainties of TE and PEU are co-minimized and give slope and aspect estimations with the highest statistical reliability.

*4) I don’t understand Figure 4. Part B illustrates conceptually how aspect values are pushed away from and towards certain angles. That is not what part A shows. Part A shows that the probability density of 91 degrees is anomalously high and that of 89 degrees is anomalously low. The same bias towards larger values just above angles that are multiples of 45 degrees applies to all other values. I don’t understand how this bias occurs but it is certainly not the result of a tendency of the algorithm to result in higher values at angles that are multiples of 45 degrees, as implied by part B.*

We are confident in the conceptual diagram shown in Part B, which is based on the magnitudes of TE shown in Figure 3. There exist regions of convergence (e.g., 45 degrees is bounded by red (+) on the left and blue (-) on the right, so values are pushed towards it) and divergence (e.g., 90 degrees). Furthermore, the magnitude of those biases is modified by the slope of the surface – there are larger aspect biases in flat areas (see Figure 3).

However, the reviewer is correct in noting that Figure 4A does not follow directly to Figure 4B – this was an oversight in the MS that we have fixed. In essence, the ‘spikes’ seen in Figure 4A show the impact of the choice of aspect bin centers, not the convergence/divergence shown in Figure 4B. As the input aspect data is on a square grid, there are naturally more pixels at the cardinal directions. As the histogram function uses half-open bins – e.g., [44,45) and [45,46) – there are significantly fewer points just below the cardinal directions (and other multiples of 45, such as 22.5, etc), and significantly more in the bin above. At the scale of our synthetic data (1001x1001 sized grid), this translates to 1-2 extra pixels in the cardinal direction bins, which create those spikes in the frequency distribution. The impact of switching from bins starting at 0 or 0.5 can be seen in Figure 2 of this reply.

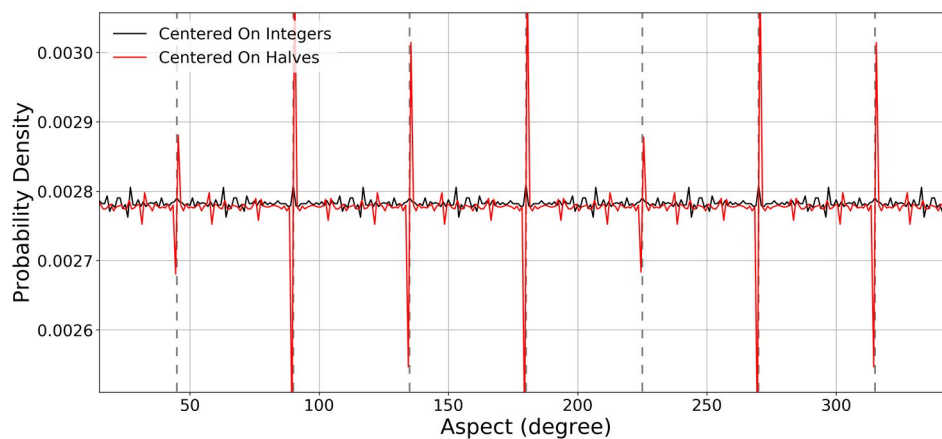


Figure 2 – Impact of bin centers. Black lines use bins centered over integer numbers (e.g., [44.5, 45.5), [45.5, 46.5)). Red lines use bins centered over halves (e.g., [44, 45), [45, 46)). While both binnings result in spikes in the aspect distributions, the very large spikes at the cardinal directions are more pronounced in the centered (red) binning.

Unfortunately, there does not exist a binning which can suppress all of the spikes in the aspect distribution of a square grid. Referring back to our original Figure 4, we only expect the effect shown in Figure 4B to manifest with very fine binnings (on the order of the error magnitudes,  $1e-4$ ), which will only be seen in very large datasets, and should not have an impact on our aspect bins at the scale of our synthetic data grid spacing. For DEMs with larger truncation errors, for example a DEM with a 10-m grid-cell size, we would, however, expect the TE to shift pixels in and out of certain aspect bins, as is suggested by Figure 3 and Figure 4B.

In light of this clarification, we have modified Figure 1, which is also influenced by the choice of bin centers, and removed Figure 4 so as not to cause confusion. We have also updated text in several places in the MS where the binning effect was misrepresented as a TE impact.

5) *The most common method for determining the appropriate scale for computing slopes and curvatures that reflect landscape-scale attributes is to plot curvature as a function of scale and identify the scaling break following Roering et al., 2010, Evidence for biotic controls on topography and soil production. I think this alternative should be mentioned. At present the paper isn't referenced.*

We have added this citation as an alternative method of choosing the appropriate scale for DEM analysis (Page 18, Line 10).

#### **Literature Cited:**

Martin Isenburg, Yuanxin Liu, Jonathan Shewchuk, Jack Snoeyink, Tim Thirion, Generating Raster DEM from Mass Points via TIN Streaming, GIScience'06 Conference Proceedings, pages 186-198, September 2006.

Rheinwalt, Aljoscha, and Bodo Bookhagen. "Network-based flow accumulation for point clouds: Facet-Flow Networks (FFN)." *Remote Sensing for Agriculture, Ecosystems, and Hydrology XX*. Vol. 10783. International Society for Optics and Photonics, 2018.

# Determining the Optimal Grid Resolution for Topographic Analysis on an Airborne Lidar Dataset

Taylor Smith<sup>1</sup>, Aljoscha Rheinwalt<sup>1</sup>, and Bodo Bookhagen<sup>1</sup>

<sup>1</sup>Institute of Earth and Environmental Sciences, Universität Potsdam, Germany

**Correspondence:** Taylor Smith (tasmith@uni-potsdam.de)

**Abstract.** Digital Elevation Models (DEMs) are a gridded representation of the surface of the earth and typically contain uncertainties due to data collection and processing. The topographic metrics slope and aspect contain errors and uncertainties inherited both from the representation of a continuous surface as a grid (referred to as truncation error, TE), and from any DEM uncertainty. We analyze in detail the impacts of TE and propagated elevation uncertainty (PEU) on slope and aspect.

5 Using synthetic data as a control, we define functions to quantify both TE and PEU for arbitrary grids. We then develop a quality metric which captures the combined impact of both TE and PEU on the calculation of topographic metrics. Our quality metric allows us to examine the spatial patterns of error and uncertainty in topographic metrics, and to compare calculations on DEMs of different sizes and accuracies.

10 Using lidar data with point density of  $\sim 10$  pts/m<sup>2</sup> covering Santa Cruz Island in southern California, we are able to generate DEMs and uncertainty estimates at several grid resolutions. Slope (aspect) errors on the one-meter dataset are on average  $0.3^\circ$  ( $0.9^\circ$ ) from TE, and  $5.5^\circ$  ( $14.5^\circ$ ) from PEU. We calculate an optimal DEM resolution for our SCI lidar dataset of four meters that minimizes the error bounds on topographic metric calculations due to the combined influence of TE and PEU for both slope and aspect calculations over the entire SCI. Average slope (aspect) errors from the four meter DEM are  $0.25^\circ$  ( $0.75^\circ$ ) from TE and  $5^\circ$  ( $12.5^\circ$ ) from PEU. While the smallest grid resolution possible from the high-density SCI lidar is not  
15 necessarily optimal for calculating topographic metrics, high point-density data are essential for measuring DEM uncertainty across a range of resolutions.

## 1 Introduction

Continuous surfaces are often projected onto an evenly sampled grid – digital elevation models (DEMs) are a common example. The accuracy of the gridded representation of the underlying surface is controlled by the spacing of the grid, the variability of  
20 the surface (i.e., the terrain itself), and the amount of uncertainty added during data collection and processing.

In recent years, an ever-growing array of DEM datasets have become available across a range of resolutions and spatial scales. As new data acquisition and processing strategies – such as lidar, stereo photogrammetry, and structure from motion – mature, the number and variability of features represented in a DEM will grow dramatically. In this manuscript, we refer to DEMs as high resolution when their grid spacing is low (e.g., one to three meters), and low resolution when their grid spacing  
25 is high (e.g., a 10+ meter DEM). Across all DEM resolutions, it is important to quantify the uncertainties in DEMs, and their

potentially large impacts on metrics calculated from the DEM (Florinsky, 1998; Zhou and Liu, 2004; Oksanen and Sarjakoski, 2005; Wechsler and Kroll, 2006; Wechsler, 2007).

The estimation of topographic metrics, such as slope and aspect, is a common task across scientific disciplines. Slope and aspect provide important boundary conditions for hillslope stability analysis (e.g., Montgomery and Dietrich, 1994; Tucker and Bras, 1998) and landslide monitoring (e.g., Guzzetti et al., 1999; Ayalew and Yamagishi, 2005), geomorphic transport laws (e.g., Roering et al., 1999; Dietrich et al., 2003; Pelletier, 2008; Grieve et al., 2016), hydrologic applications (e.g., Band, 1986; Zhang and Montgomery, 1994; Tarboton, 1997; Pelletier, 2010, 2013) including flood risk modeling (e.g., Ouma and Tateishi, 2014) and stream power analysis (e.g., Bookhagen and Strecker, 2012; Lague, 2014), tectono-geomorphic modeling (e.g., Whipple and Tucker, 1999; Snyder et al., 2000; Tucker and Hancock, 2010; Kirby and Whipple, 2012; Bookhagen and Strecker, 2012), ecologic modeling (e.g., Franklin, 1995; Guisan and Zimmermann, 2000; Thompson et al., 2001), and vegetation analysis (e.g., Pierce et al., 2005; Kent, 2011).

A wide range of methods have been developed to accurately derive slope and aspect from elevation data using a range of approaches, each optimized for different use cases (e.g., Evans, 1980; Zevenbergen and Thorne, 1987; Skidmore, 1989; Tarboton, 1997; Dunn and Hickey, 1998; Schmidt et al., 2003). For example, the methods D-8 and D-Infinity are optimized towards hydrologic flow-routing problems, particularly on DEMs of low spatial resolution (Tarboton, 1997), and the methods of Evans (1980) and Zevenbergen and Thorne (1987) include some smoothing of the underlying DEM to minimize the impacts of DEM noise. However, all of these methods contain some intrinsic error due to truncation error (TE) – the deviation of the gridded sample from the continuous original surface (Figure 1). The TE describes the error made by truncating an infinite sum and approximating it by a finite sum. It often includes a discretization error, which arises from taking a finite number of steps to approximate an continuous surface. Several authors have explored the theoretical limitations of estimations of slope and aspect calculations on gridded surfaces (e.g., Heuvelink et al., 1989; Hunter and Goodchild, 1997; Florinsky, 1998; Abarbanel et al., 2000; Zhou and Liu, 2004); in general, TE can be related directly to the grid-sampling – more tightly sampled grids will deviate less from the original surface.



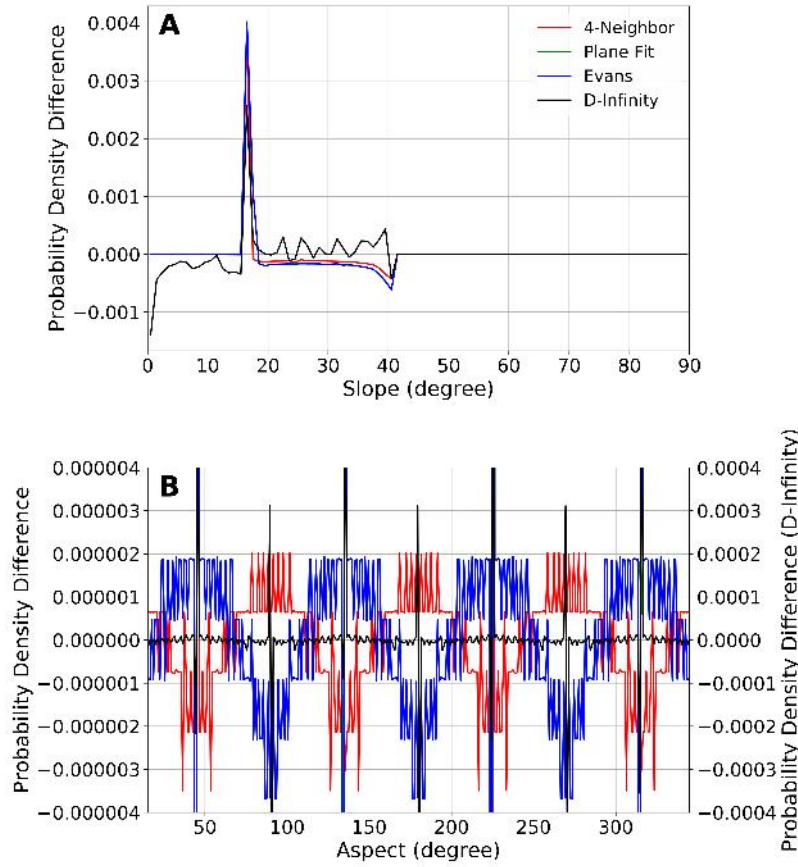


**Figure 1.** (A) Slope and (B) aspect distribution differences from analytical solutions of slope and aspect on a Gaussian Hill, on one-degree bins, starting from [0.5, 1.5). None of the methods perfectly match the analytical solution, with slightly different offset magnitudes. ~~In particular, each~~ Note that the D-Infinity method (black line) produces aspect frequency distribution errors at two orders of magnitude larger than those errors produced by the cardinal directions other methods. It is important to note, however, that the aspect offsets are small – on the order of 1-5 pixels per bin for the methods excluding D-Infinity.

In addition to TE, real-world DEMs will have some degree of measurement uncertainty. The magnitude of that uncertainty varies across data collection methods and data post-processing, but also depends on the terrain itself and is often difficult to estimate (Heuvelink et al., 1989; Lee et al., 1992; Bolstad and Stowe, 1994; Florinsky, 1998; Fisher, 1999; Smith and Sandwell, 2003; Farr et al., 2007; Wechsler and Kroll, 2006; Wechsler, 2007; Mukul et al., 2017; Purinton and Bookhagen, 2017, 2018; Wessel et al., 2018). Any uncertainty in elevation estimates will propagate into the calculated topographic metrics.

The impacts of TE and DEM uncertainty on slope and aspect estimations can be quantified for any gridded data. We first use synthetic data with known properties as a control to define generalized functions applicable to any DEM, and to develop a quality metric for slope and aspect calculations. Following this analysis, we turn to a high-resolution lidar dataset covering complex terrain to study the spatial structure of uncertainty in topographic metrics propagating from both TE and DEM

uncertainty. This novel approach allows us to identify the optimal grid resolution that minimizes the error bounds from the combination of TE and PEU, and to analyze the implications of using sub-optimal DEM resolutions for calculating slope and aspect.

## 2 Data and Methods

5 In this analysis, we demonstrate the limitations of calculating slope and aspect using synthetic data surfaces. These surfaces serve as a valuable control dataset, as the precise analytical values for slope and aspect at each grid cell are known. We further add normally distributed random noise with a known mean and standard deviation to our synthetic data to investigate the impacts of DEM uncertainty on topographic metrics. Following the discussion of synthetic data, we apply the same methods to high-resolution lidar data interpolated to DEMs with varying spatial resolutions.

### 10 2.1 Synthetic Data

We generate regular  $n \times n$  grids of size  $n=11, 101, 1001$  describing a Gaussian hill with a maximum height of one, with elevations defined on a regular square grid as  $z = e^{(-x^2-y^2)}$  for each  $(x,y)$  grid cell (Figure 2). A second surface describing a sphere is included in the Supplement. It is important to note that the horizontal and vertical units for the synthetic data are arbitrary – the grid cell spacings generated by using differently sized grids are an expression of the width-to-height ratio of the surface. The python functions used to generate our synthetic surfaces can be found on GitHub: <https://github.com/UP-RS-ESP/TopoMetricUncertainty/surfaces.py>.

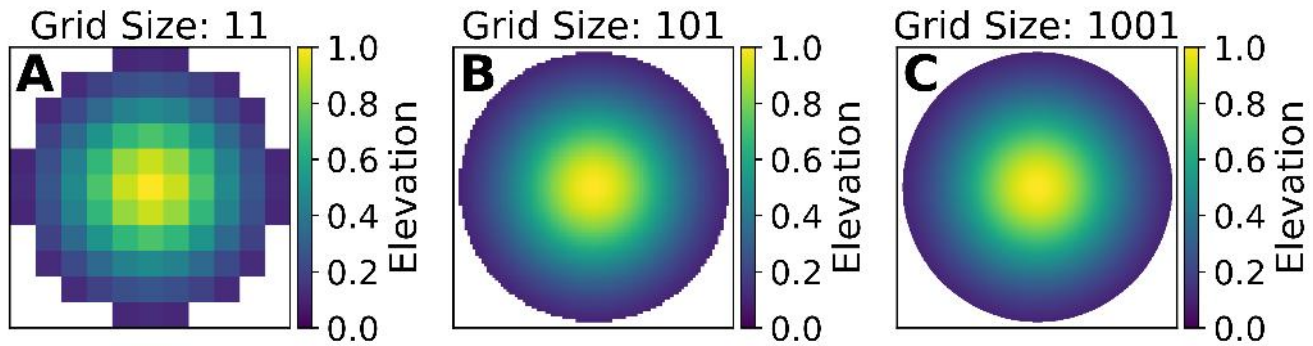


**Figure 2.** Gaussian hill elevations at  $n=11, 101$ , and  $1001$ . As grid sizes increase, a smoother surface is generated. Note that the horizontal and vertical units are arbitrary and that the grid-cell spacings are an expression of the width-to-height ratio of the surface. Cross sections of the shapes at all grid sizes can be seen in Supplemental Figure 1.

## 2.2 Topographic Metrics

In this study, we focus on the topographic metrics slope  $S(x, y)$  and aspect  $A(x, y)$  which we define as,

$$S(x, y) = \frac{180^\circ}{\pi} \times \arctan \sqrt{\left(\frac{\partial z}{\partial x}\right)^2 + \left(\frac{\partial z}{\partial y}\right)^2} \quad (1)$$

and

$$A(x, y) = \frac{180^\circ}{\pi} \times \arctan \left( \frac{\partial z}{\partial y} \times \frac{\partial x}{\partial z} \right) + 180^\circ \quad (2)$$

with  $x$  and  $y$  being the spatial coordinates. Key in calculating slope and aspect is the calculation of the directional derivatives  $\frac{\partial z}{\partial x}$  and  $\frac{\partial z}{\partial y}$ .

There exist a wide range of methods for calculating the directional derivatives on gridded data that broadly fall into three classes: (1) four-neighborhood methods, (2) eight-neighborhood methods, and (3) steepest descent methods (e.g. Evans, 1980; Zevenbergen and Thorne, 1987; Skidmore, 1989; Tarboton, 1997; Dunn and Hickey, 1998; Schmidt et al., 2003; Zhou and Liu, 2004; Oksanen and Sarjakoski, 2005). In our analysis, we use the standard second-order finite difference approximation as implemented in Python Numpy (Fornberg, 1988; Durran, 1999), which is a four-neighborhood method. We tested additional methods using eight-neighborhoods (e.g., singular-value decomposition plane fitting and the method of Evans (1980)) – which provide some underlying DEM-smoothing and are well-suited to noisy DEM data – and using steepest descent (e.g., D-8 and D-Infinity (Tarboton, 1997)), which identify the steepest slope that water would take and are optimized for hydrologic use cases. However, these methods do not necessarily provide the most representative slope of the terrain, and show distinct differences from the analytical solutions of slope and aspect (cf. Supplemental Figures 2 and 3). We choose to use the simple four-neighbor method in our analysis as it results in the lowest relative error when compared with the analytical solution for slope and aspect (Supplemental Figure 2) and does not include any smoothing of the underlying DEM.

## 3 Sources of Uncertainty in Topographic Metrics

Biases in topographic metrics can be determined both numerically, by comparing the results of calculations to known values, and analytically, by deriving the impacts of both TE and DEM uncertainty on topographic metrics.

### 3.1 Truncation Error

We derive the TE from the formulas of topographic metrics by propagating the uncertainty of the second-order finite difference approximation for the directional derivatives  $\frac{\partial z}{\partial x}$  and  $\frac{\partial z}{\partial y}$ . Neglecting rounding errors, we assume the uncertainty  $\varepsilon$  of the second-order finite difference  $\Delta$  to be bounded by

$$\left| \frac{\partial z}{\partial a} - \Delta z_a \right| \equiv \left| \frac{\partial z}{\partial a} - \frac{z(a+h) - z(a-h)}{2h} \right| \lesssim \frac{h^2}{6} \left| \frac{\partial^3 z}{\partial a^3} \right| = \varepsilon_a \quad (3)$$

where  $a$  represents either  $x$  or  $y$ , and  $h$  is the grid spacing.

The considered topographic metrics slope  $S(x, y)$  and aspect  $A(x, y)$  depend on both directional derivatives  $\frac{\partial z}{\partial x}$  and  $\frac{\partial z}{\partial y}$ . As the corresponding uncertainties  $\varepsilon_x$  and  $\varepsilon_y$  are not independent, propagated TE  $T$  for slope ( $T_S$ ) and aspect ( $T_A$ ) are given by

$$|T_S(x, y)| = \sqrt{\left(\frac{\partial \frac{\partial z}{\partial x} S}{\partial x}\right)^2 \varepsilon_x^2 + \left(\frac{\partial \frac{\partial z}{\partial y} S}{\partial y}\right)^2 \varepsilon_y^2 + 2 \left(\frac{\partial \frac{\partial z}{\partial x} S}{\partial x}\right) \left(\frac{\partial \frac{\partial z}{\partial y} S}{\partial y}\right) \varepsilon_x \varepsilon_y} \sqrt{\left(\frac{\partial S}{\partial \Delta z_x}\right)^2 \varepsilon_x^2 + \left(\frac{\partial S}{\partial \Delta z_y}\right)^2 \varepsilon_y^2 + 2 \left(\frac{\partial S}{\partial \Delta z_x}\right) \left(\frac{\partial S}{\partial \Delta z_y}\right) \varepsilon_x \varepsilon_y} \quad (4)$$

$$5 \quad |T_A(x, y)| = \sqrt{\left(\frac{\partial \frac{\partial z}{\partial x} A}{\partial x}\right)^2 \varepsilon_x^2 + \left(\frac{\partial \frac{\partial z}{\partial y} A}{\partial y}\right)^2 \varepsilon_y^2 + 2 \left(\frac{\partial \frac{\partial z}{\partial x} A}{\partial x}\right) \left(\frac{\partial \frac{\partial z}{\partial y} A}{\partial y}\right) \varepsilon_x \varepsilon_y} \sqrt{\left(\frac{\partial A}{\partial \Delta z_x}\right)^2 \varepsilon_x^2 + \left(\frac{\partial A}{\partial \Delta z_y}\right)^2 \varepsilon_y^2 + 2 \left(\frac{\partial A}{\partial \Delta z_x}\right) \left(\frac{\partial A}{\partial \Delta z_y}\right) \varepsilon_x \varepsilon_y} \quad (5)$$

These can be more explicitly expressed using Equation (3) as

$$|T_S(x, y)| = \frac{180^\circ}{\pi} \times \sqrt{\frac{\left(\frac{\partial z}{\partial x}\right)^2 \varepsilon_x^2 + \left(\frac{\partial z}{\partial y}\right)^2 \varepsilon_y^2 + 2 \frac{\partial z}{\partial x} \frac{\partial z}{\partial y} \varepsilon_x \varepsilon_y}{\left(\frac{\partial z}{\partial x} + \frac{\partial z}{\partial y}\right) \left(1 + \frac{\partial z}{\partial x} + \frac{\partial z}{\partial y}\right)^2}} \sqrt{\frac{\Delta z_x^2 \varepsilon_x^2 + \Delta z_y^2 \varepsilon_y^2 + 2 \Delta z_x \Delta z_y \varepsilon_x \varepsilon_y}{(\Delta z_x + \Delta z_y) (1 + \Delta z_x + \Delta z_y)^2}} \quad (6)$$

$$|T_A(x, y)| = \frac{180^\circ}{\pi} \times \sqrt{\frac{\left(\frac{\partial z}{\partial x}\right)^2 \varepsilon_x^2 + \left(\frac{\partial z}{\partial y}\right)^2 \varepsilon_y^2 - 2 \frac{\partial z}{\partial x} \frac{\partial z}{\partial y} \varepsilon_x \varepsilon_y}{\left(\frac{\partial z}{\partial x}\right)^4 \left(1 + \frac{\partial z}{\partial x} + \frac{\partial z}{\partial y}\right)^2}} \sqrt{\frac{\Delta z_x^2 \varepsilon_x^2 + \Delta z_y^2 \varepsilon_y^2 - 2 \Delta z_x \Delta z_y \varepsilon_x \varepsilon_y}{\Delta z_x^4 (1 + \Delta z_x + \Delta z_y)^2}} \quad (7)$$

The sign of the TE is derived from symmetry considerations in the following way:

$$10 \quad \text{sign}(T_S) = \text{sign} \left( \arctan \sqrt{\left(\frac{\partial z}{\partial x} + \varepsilon_x\right)^2 + \left(\frac{\partial z}{\partial y} + \varepsilon_y\right)^2} \sqrt{(\Delta z_x + \varepsilon_x)^2 + (\Delta z_y + \varepsilon_y)^2} \right. \\ \left. - \arctan \sqrt{\left(\frac{\partial z}{\partial x} - \varepsilon_x\right)^2 + \left(\frac{\partial z}{\partial y} - \varepsilon_y\right)^2} \sqrt{(\Delta z_x - \varepsilon_x)^2 + (\Delta z_y - \varepsilon_y)^2} \right) \quad (8)$$

and

$$\text{sign}(T_A) = \text{sign} \left( \arctan \frac{\frac{\partial z}{\partial y} + \varepsilon_y}{\frac{\partial z}{\partial x} + \varepsilon_x} \frac{\Delta z_y + \varepsilon_y}{\Delta z_x + \varepsilon_x} - \arctan \frac{\frac{\partial z}{\partial y} - \varepsilon_y}{\frac{\partial z}{\partial x} - \varepsilon_x} \frac{\Delta z_y - \varepsilon_y}{\Delta z_x - \varepsilon_x} \right) \quad (9)$$

Equations 6-9 allow us to calculate the magnitude of the TE at each point  $(x, y)$  on our synthetic surfaces (Figure 3).

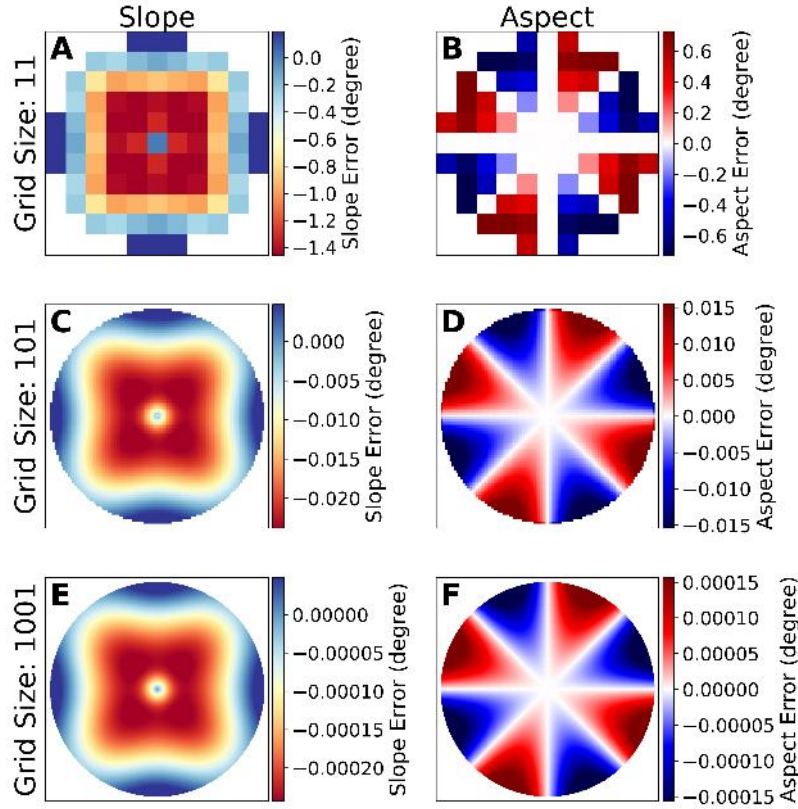


**Figure 3.** Gaussian hill slope (A, C, E) and aspect (B, D, F) errors from the analytical TE. All grid sizes show clear spatial patterns in slope and aspect errors. Offset magnitudes scale with grid size. Errors on the  $n=1001$  grid (bottom row: E, F) are generally two orders of magnitude smaller than those for the  $n=101$  grid (middle row: C, D). Colors scaled from 5th to 95th percentiles of error magnitudes.

As can be seen in Figure 3, the magnitude of the slope and aspect error decreases with increasing  $n$ . This implies that as more tightly sampled models of a surface are used, the accuracy of slope and aspect estimations increases. This follows the work of Abarbanel et al. (2000), which shows that finite-difference derivative estimations have error magnitudes that scale with the inverse of the grid spacing for evenly spaced grids. However, even with increasingly accurate surface models, there remains some TE simply due to the fact that a smooth surface cannot be perfectly represented by gridded data. At very fine scales, computer rounding will also lead to errors in slope and aspect calculations. In this study, however, we do not use fine enough grids for this to impact our error estimates.

As the precise mathematical definitions of our synthetic surfaces are known, we can analytically derive their slope and aspect values at each point and compare those results to numerical calculations (see Supplemental Figure 4). In the absence of DEM uncertainty, the difference between analytically- and numerically-derived topographic metrics will be dominated by the TE from the second-order finite difference approximation. Additionally, modifying the absolute magnitude of the shape



heights (e.g., a maximum height of 100 instead of one), does not modify the absolute magnitudes of slope and aspect TE (see Supplemental Figure 5).

~~While the magnitudes of the errors are small, they have important impacts on distributions drawn from larger grids (e.g., entire surfaces, see Figure ??). In the case of aspect, the alternating spatial pattern of its TE pushes aspect values towards the cardinal directions — leading to distinct positive and negative spikes in the aspect distribution. This error is not confined only to the cardinal directions — there exists symmetry across the aspect distribution that is easiest to see with very fine binning (see Supplemental Figure 6).~~

~~(A) Density histogram of synthetic data ( $n=1001$ ) using the four-neighbor method, on one-degree bins. Spikes clearly occur around the cardinal directions. The symmetry across the aspect distributions can be further explored in the Supplemental Figure 5 with very fine binning. (B) Conceptual diagram of aspect errors. Aspect values are pushed towards and away from certain angles (0/45/90/etc).~~

Slope and aspect calculations have very different spatial error patterns (see Figure 3). However, as with aspect errors, slope errors depend on the orientation of the grid despite the radial symmetry of the surface. This is easiest to see in the slope difference map of the Gaussian hill, where error magnitudes are not simply scaled by slope (see Figure 3E).

### 3.2 DEM Uncertainty

Elevation models are never perfect – there are always errors and uncertainties due to data collection or processing. The uncertainty in calculated topographic metrics can be constrained by propagating DEM uncertainties into their calculations (e.g. Heuvelink et al., 1989; Hunter and Goodchild, 1997; Zhou and Liu, 2004; Oksanen and Sarjakoski, 2005); we refer to the uncertainty introduced into slope and aspect calculations from elevation uncertainty as propagated elevation uncertainty (PEU).

For our synthetic data, we assume the simplistic but straight forward error model of spatially uncorrelated white noise. We define noise to be normally distributed and consider two cases: (1) homogeneous white noise, i.e., noise drawn from one unique normal distribution  $\mathcal{N}(\mu = 0, \sigma^2 = \text{const})$ , and (2) slope dependent, spatially varying white noise, i.e., noise drawn from a family of normal distributions  $\mathcal{N}(\mu = 0, \sigma_S^2)$ . Since for each grid cell noise is drawn independently, the PEU for slope ( $E_S$ ) and aspect ( $E_A$ ) is given by

$$E_S = \sqrt{\sum_{i \in \{x-h, x+h\}} \sum_{j \in \{y-h, y+h\}} \left( \frac{\partial S}{\partial z_{ij}} \right)^2 \sigma_{z_{ij}}^2} \quad (10)$$

$$E_A = \sqrt{\sum_{i \in \{x-h, x+h\}} \sum_{j \in \{y-h, y+h\}} \left( \frac{\partial A}{\partial z_{ij}} \right)^2 \sigma_{z_{ij}}^2} \quad (11)$$

As before, this can be expressed more explicitly using Equation (3) as

$$E_S = \frac{90^\circ}{h\pi} \sqrt{\frac{\left(\frac{\partial z}{\partial x}\right)^2 (\sigma_{z_{x+h,y}}^2 + \sigma_{z_{x-h,y}}^2) + \left(\frac{\partial z}{\partial y}\right)^2 (\sigma_{z_{x,y+h}}^2 + \sigma_{z_{x,y-h}}^2)}{\left(\left(\frac{\partial z}{\partial x}\right)^2 + \left(\frac{\partial z}{\partial y}\right)^2\right) \left(1 + \left(\frac{\partial z}{\partial x}\right)^2 + \left(\frac{\partial z}{\partial y}\right)^2\right)^2}} \sqrt{\frac{\Delta z_x^2 (\sigma_{z_{x+h,y}}^2 + \sigma_{z_{x-h,y}}^2) + \Delta z_y^2 (\sigma_{z_{x,y+h}}^2 + \sigma_{z_{x,y-h}}^2)}{(\Delta z_x^2 + \Delta z_y^2) \left(1 + \Delta z_x^2 + \Delta z_y^2\right)^2}} \quad (12)$$

$$E_A = \frac{90^\circ}{h\pi} \sqrt{\frac{\left(\frac{\partial z \partial x}{\partial y \partial z}\right)^2 (\sigma_{z_{x+h,y}}^2 + \sigma_{z_{x-h,y}}^2) + \sigma_{z_{x,y+h}}^2 + \sigma_{z_{x,y-h}}^2}{\left(\frac{\partial z}{\partial x}\right)^2 \left(1 + \left(\frac{\partial z \partial x}{\partial y \partial z}\right)^2\right)^2}} \sqrt{\frac{\left(\frac{\Delta z_y}{\Delta z_x}\right)^2 (\sigma_{z_{x+h,y}}^2 + \sigma_{z_{x-h,y}}^2) + \sigma_{z_{x,y+h}}^2 + \sigma_{z_{x,y-h}}^2}{\Delta z_x^2 \left(1 + \left(\frac{\Delta z_y}{\Delta z_x}\right)^2\right)^2}} \quad (13)$$

As with TE, PEU introduces distinctive spatial patterns into the slope and aspect estimates (Figure 4). Both slope and aspect uncertainties are higher on shallow slopes, as has been shown in previous work (Florinsky, 1998; Zhou and Liu, 2004). On flat or nearly flat terrain, the elevation uncertainty will more strongly impact the estimated partial derivatives, and thus lead to erroneous slope and aspect estimates. It is also important to note that aspect varies between  $[0, 360)$  and slope only between  $[0, 90)$ , which is why we expect standard deviations to be different by a factor of four (see Figure 4).

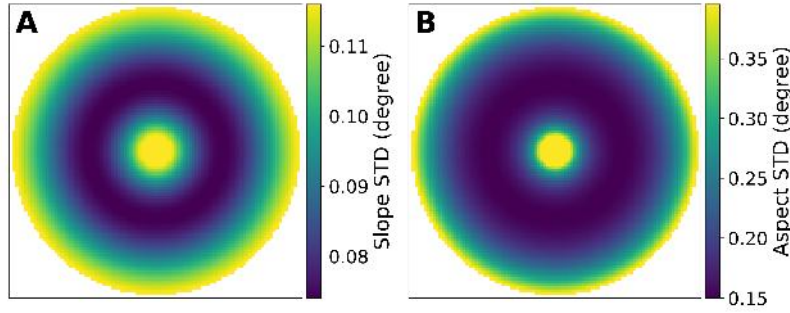


**Figure 4.** Gaussian hill ( $n=101$ ) slope and aspect standard deviations for spatially invariant noise ( $\text{std}=1e^{-4}$ ), derived from elevation uncertainty propagation (Equations 12-13). Aspect has higher standard deviations than slope, as aspect varies between  $[0, 360)$  and slope only between  $[0, 90)$ . This is evident especially on flat terrain (e.g., the edges of the Gaussian hill).

When we compare our analytically-derived topographic metric uncertainty patterns (Figure 4) to those generated from actual random noise – using an ensemble of 10,000 synthetic surfaces, each generated with normally distributed noise – the spatial patterns and magnitudes are nearly identical between the two methods (cf. Supplemental Figure 76).

#### 4 Optimal Grid Spacing

Both TE and PEU yield distinct spatial patterns, implying that the error and uncertainty in topographic metrics will vary throughout a DEM. Using both the TE and PEU magnitudes, we can examine whether TE or PEU is dominant at an arbitrary grid spacing, given a known DEM uncertainty (Figure 5).

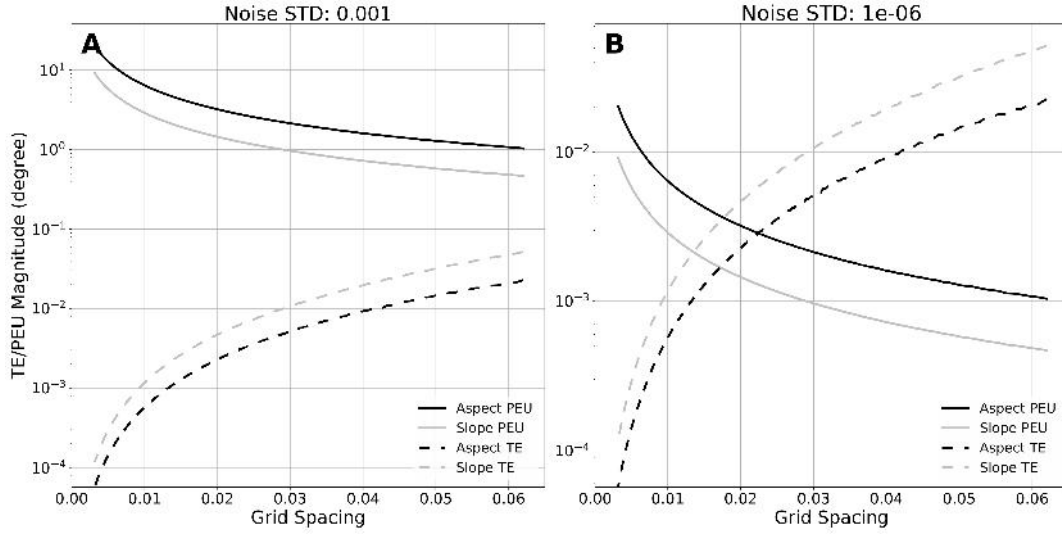


**Figure 5.** TE and PEU magnitudes for two noise levels, (A)  $1e^{-4}$  and (B)  $1e^{-6}$ , compared to grid spacing. Aspect plotted in black, slope plotted in gray. Solid lines for PEU, dashed lines for TE. TE decreases with decreasing grid spacing, while PEU increases as the noise standard deviation relative to grid spacing increases.

As can be seen in Figure 5, TE will approach zero for sufficiently small grid spacings, while PEU will rise as the amount of noise relative to the grid spacing increases. Using both TE and PEU magnitudes across grid spacings, an optimal grid spacing for a given noise level which minimizes their combined influence can be chosen. Note that we do not assume that the quality of the data is maximized when the combination of TE and PEU is minimized, but that the error bounds on topographic metric calculations are minimized. Thus, the optimal grid spacing is preferred for calculating slopes and aspects for use in applications where uncertainty across the entire grid should be minimized.

#### 4.1 Metric Quality Ratios

The trade off between TE and PEU can also be thought of as a quality ratio. Simply put, the impact of DEM uncertainty on topographic metrics is modulated by the grid spacing – i.e., 1 cm of vertical noise on a 10 m grid will have a very different impact than 1 cm of vertical noise on a 1 cm grid. As both TE and PEU have distinct spatial patterns, a combined Quality Ratio (QR) can capture a holistic view of the overlapping influence of TE and PEU. The QR can be defined from the combination of the TE and PEU as:

$$QR = \left( \frac{1}{1 + (m \times |TE|)} \right) \times \left( \frac{1}{1 + (m \times |PEU|)} \right) \quad (14)$$

where  $m$  is a normalization factor which accounts for the four-fold difference in the range of possible values between slope and aspect. On a surface without noise, the QR will approach one as grid spacing and TE approach zero. The influence of TE

and PEU on calculated QRs can be seen by comparing the same synthetic grid with two noise levels (see Supplemental Figure 87). High noise levels reveal similar spatial patterns to those seen in Figure 4, while low noise levels show the influence of TE (cf. Figure 3).

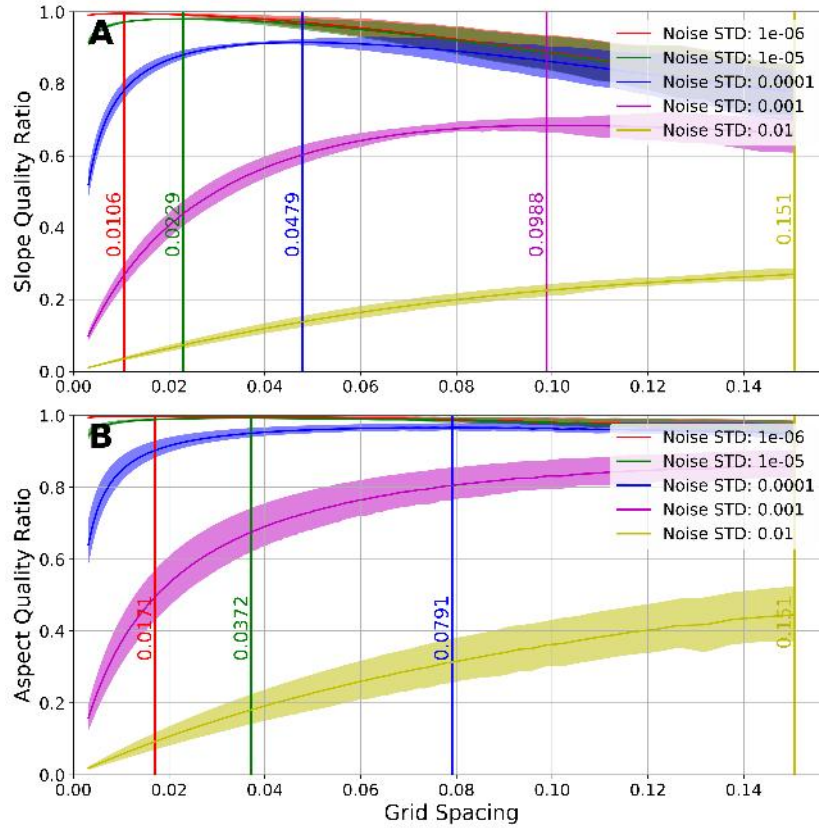


**Figure 6.** Gaussian hill slope (A, top) and aspect (B, bottom) QRs vs grid spacings, for a range of noise levels ( $1e^{-2}$  to  $1e^{-6}$ ). 25th-75th percentile QRs shaded for each noise level. Optimal grid spacings (maximum QR) for each noise level are marked with vertical lines. Slope calculations result in lower optimal grid spacings compared to aspect. Higher noise levels lead to higher optimal grid spacings for both slope and aspect calculations. Note that the purple and yellow lines in panel B have the same optimal grid spacing, and thus only the yellow line is visible.

The QR can also be used as a normalized metric to compare DEMs across grid spacings and noise levels (Figure 6, and Supplemental Figure 98). Each noise level/grid spacing pair has a point at which the QR of the DEM is maximized. This point represents the optimal trade off between TE and PEU over the entire grid.

As can be seen in Figure 6, as noise levels increase, the optimal grid spacing increases, and the QR of that optimal spacing decreases. For very noisy datasets (purple and yellow lines, Figure 6), very large grid cell spacings – i.e., aggregation – can help reduce the combined influence of TE and PEU on slope and aspect estimates.

There are distinct differences between the optimal slope and aspect grid spacings for the same dataset. For any given noise level, the optimal grid spacing to calculate aspect is higher than that for slope. The difference in optimal grid spacing is driven by the relative magnitudes of the PEU between slope and aspect calculations – the PEU for aspect calculations is always higher than that for slope due to differences in the formulas for slope and aspect (see Figure 5 and Equations 12-13).

## 5 4.2 Heterogeneous Noise

In practice, datasets will not have homogeneous noise across grid spacings – coarser parameterizations of a surface will include more uncertainty as fine-scale features are aggregated into single pixels. Additionally, noise in real-world datasets is influenced by non-uniform landscape features such as slope, aspect, terrain relief, and vegetation cover (e.g., Kraus and Pfeifer, 1998; Kyriakidis et al., 1999; Holmes et al., 2000; Smith and Sandwell, 2003; Carlisle, 2005; Oksanen and Sarjakoski, 2006; Rodriguez et al., 2006; Shortridge and Messina, 2011; Purinton and Bookhagen, 2017, 2018). While several authors (e.g., Hunter and Goodchild, 1997; Zhang and Goodchild, 2002; Fisher and Tate, 2006) have examined complex error models in real data, we choose to use a simplistic error model based on terrain slope – e.g., higher slopes have higher noise levels – to look at the first-order impacts of heterogeneous noise on the calculation of topographic metrics.

When we compare the heterogeneous noise result to the analysis shown in Figure 6 (cf. Supplemental Figure 109), the results are very similar, albeit with higher optimal grid spacings. We can also compare the optimal grid spacings for homogeneous and heterogeneous noise directly for a set of noise levels from  $1e^{-8}$  to  $1e^{-2}$  (Figure 7).



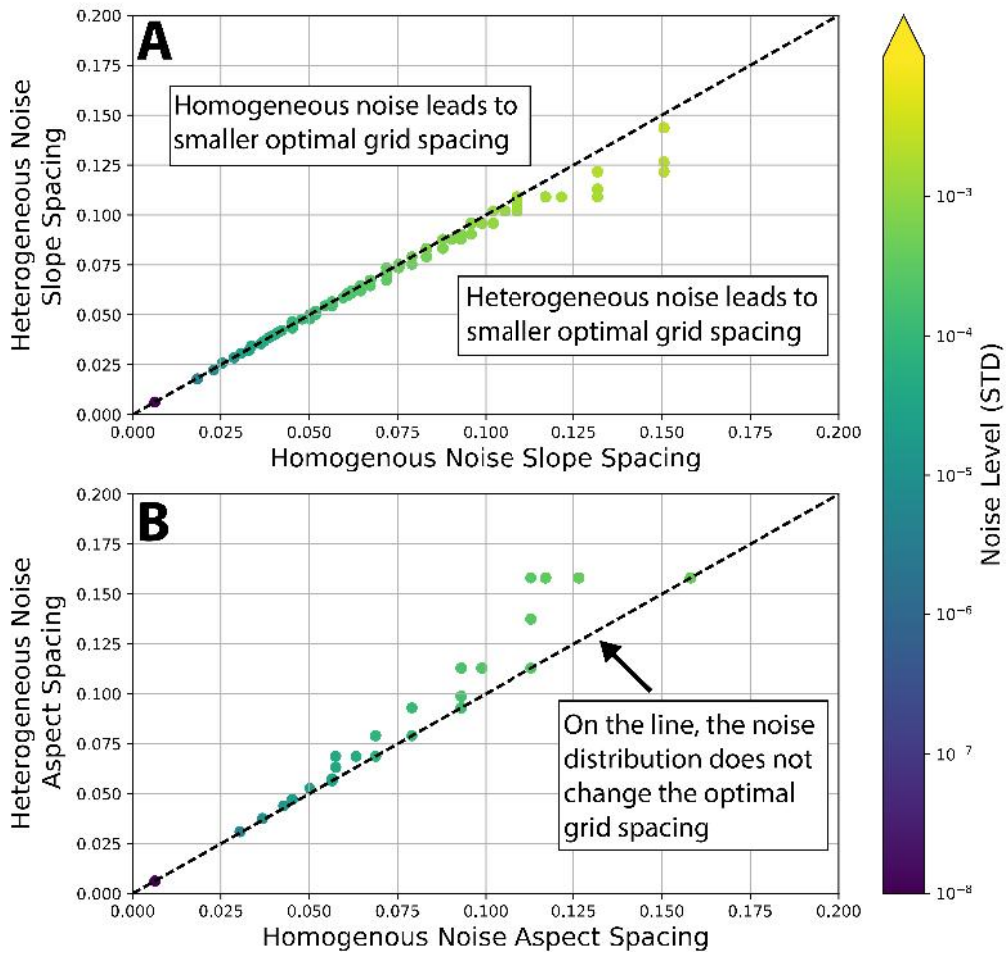


**Figure 7.** Optimal grid spacing for slope (A) and aspect (B) across a range of noise levels ( $1e^{-2}$  to  $1e^{-8}$ ). Points in the upper triangle have smaller optimal grid spacings with homogeneous noise. Points in the lower triangle have smaller optimal grid spacings with heterogeneous noise. Points on the dashed line have the same optimal grid spacings regardless of the noise distribution. Heterogeneous noise leads to smaller slope grid spacings but larger aspect spacings for the same average noise level.

As can be seen from Figure 7, slope can be calculated on a smaller grid spacing with slope-biased noise, while aspect should be calculated with a larger grid spacing. The divergence in the optimal grid spacings between homogeneous and heterogeneous noise ~~are~~ is driven by the differences in the influence of terrain slope on slope and aspect QRs. While both slope and aspect calculations have similar grid-spacing dependent TE magnitudes, the differences in the relative magnitudes of the PEU lead to different responses to the distribution of noise on the DEM (see Figure 5). The simplistic slope-dependent error model used here is unlikely to translate to a real-world setting; however, it is clear that the spatial distribution of noise on the DEM influences the choice of optimal grid spacing for both slope and aspect calculations.

## 5 Impacts of Noise on Topographic Distributions

As can be seen in Figures 4-6, the introduction of noise has non-trivial impacts on slope and aspect calculations. ~~As was evident in Figures 1 and ??, TE can significantly modify the ensemble distributions of topographic metrics.~~ To examine the impact of both TE and PEU on the frequency distributions of slope and aspect, we generate 1,000 member ensembles of slope and aspect for each combination of two different grid sizes ( $n=101, 1001$ ) and three different noise levels (homogeneous noise,  $\text{std}=1e^{-2}, 1e^{-3}, 1e^{-4}$ ). We then bin the ensemble data into one-degree slope and aspect bins.

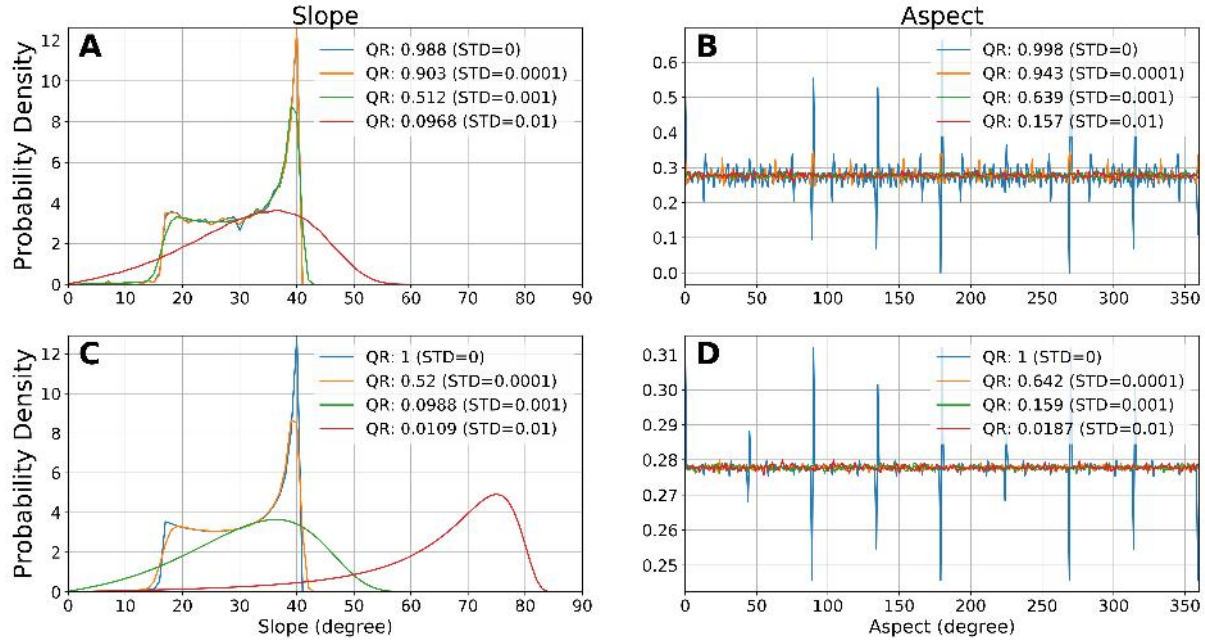


**Figure 8.** Slope (A, C) and Aspect (B, D) probability distributions (one-degree bins) for a Gaussian hill with homogeneous noise at variable levels ( $\text{std}=0, 1e^{-2}, 1e^{-3}, 1e^{-4}$ ) for  $n=101$  (A, B) and  $n=1001$  (C, D). The introduction of small levels of noise washes the spikes out of the aspect distribution. Slope distributions are steeper with the introduction of higher noise levels. Similar density functions are generated at similar QRs, despite differences in absolute noise levels.

When homogeneous noise is added to synthetic surfaces, the large spikes in aspect distributions related to ~~points moving in and out of the~~ cardinal directions (e.g., at 45/90/135 degrees, ~~see Figure ??~~) are smoothed out into neighboring bins. However, this does not imply that the calculated aspects are ‘better’, just that they have a more even distribution – the PEU overprints the TE as seen in Figure 3. This can clearly be seen in Supplemental Figure ~~H~~10, which shows the impact of noise on slope and aspect grids.

Slope distributions are systematically shifted towards higher values as more noise is added to the synthetic surfaces. This effect is due to the presence of more large ‘steps’ in the synthetic data, where smooth transitions across elevation gradients are replaced with more stepped hills and dips. Across noise levels and grid sizes, distributions with similar QRs maintain the same

general shape. This indicates that the QR captures how ‘wrong’ the aggregate distribution is when compared to the original synthetic surface.

If different window sizes are used to calculate slope and aspect (e.g., 5x5 and 7x7), slope estimates are higher and the aspect ‘spikes’ at cardinal directions are slightly diminished. Larger window sizes ~~somewhat—but not completely—remove~~  
5 ~~the impacts of noise on aspect distributions. They~~ do not, however, help minimize differences in the slope distributions (see Supplement Figure ~~4211~~).

## 6 Case Study: Multi-Resolution Lidar on Santa Cruz Island

### 6.1 Dataset Description

The Santa Cruz Island (SCI, see Figure 9) is part of the Channel Islands off the coast of south-central California. It is a tectonically active island (Neely et al., 2017) with steep topography and pronounced erosion (Perroy et al., 2010, 2012),  
5 diverse lithologic cover (Dibblee, 2001), and moderate and species-rich vegetation cover (Baguskas et al., 2014). The lidar point cloud data used to derive DEMs at a range of spatial resolutions were obtained from the 2010 US Geological Survey Channel Islands Lidar Collection (OpenTopography, 2012). The point cloud has an average point ground-classified density of  $\sim 10$  points/m<sup>2</sup>.

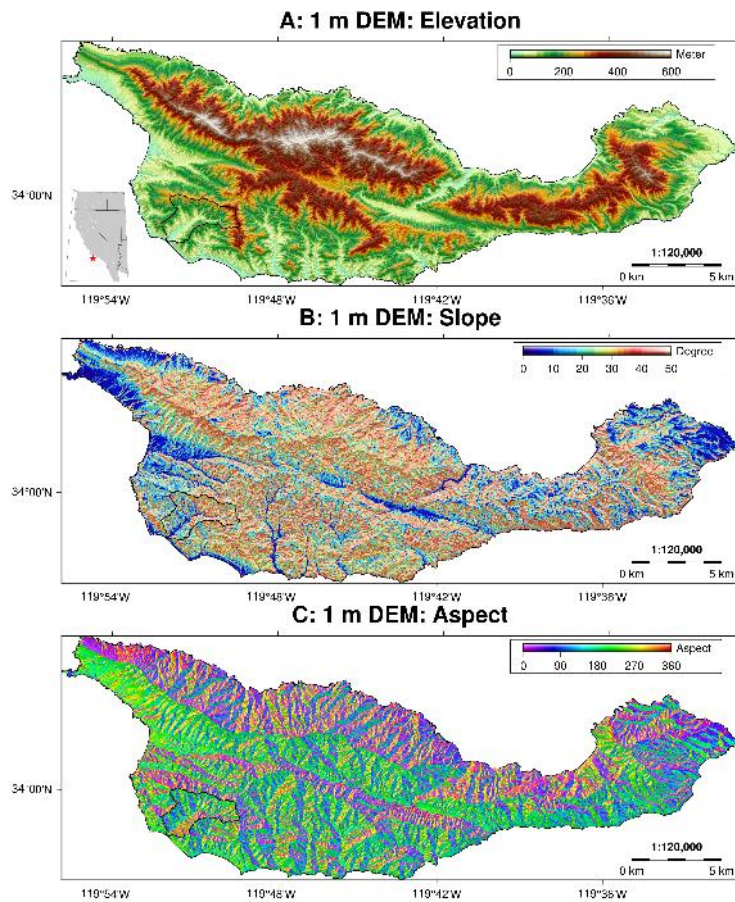


**Figure 9.** Topographic setting of Santa Cruz Island (SCI), showing elevation (A), slope (B) and aspect (C) derived from a 1-m DEM and calculated from a total of  $2.3 \times 10^9$  ground-classified lidar points. The SCI covers a wide range of terrain types, slope regimes, and all aspect directions. Black polygon (southwest SCI) indicates the Pozo catchment shown in Figure 10. For a canopy height model, we refer to Supplemental Figure [13](#).[12](#).

## 6.2 Deriving Elevations and Uncertainties from Point Cloud Data

Using LAStools (LAStools, 2017), we use a triangulated irregular network (TIN) approach to derive average point cloud elevations at each grid cell center, for each of our chosen grid resolutions (1-30 meters, in one meter steps, and 90 meters). We have tested ~~simpler interpolation schemes, including the lowest elevation and the central location for each grid cell, but the resulting uncertainties in topographic metrics remain the same. Thus, we decided to use the more commonly applied triangulated irregular network approach.~~ several alternative interpolation schemes – including simple means, inverse-distance weights, and other triangulation schemes – using all of the major open source software packages (see Supplemental Table 1 for a full listing, and Supplemental Figures 13-21 for a cross-comparison). Each of these methods generates a slightly different DEM, with different assumptions and ideal use cases. Our optimal grid resolution analysis is applicable to each of these DEMs; there is relatively little variation in grid-wide TE and PEU across interpolation schemes. To simplify our discussion of the lidar data, we use only the TIN DEM for further analysis. However, it is clear that our analysis of TE and PEU for slope and aspect are equally applicable to DEMs created with alternative interpolation schemes.

In addition to producing DEMs, we generate pixel-wise standard deviations estimated from the point cloud. That is, we determined the standard deviation of all ground-classified lidar points falling into each grid cell for each grid resolution. While vegetation cover may impact ground-classification results, our calculations are based on ground-classified points only. Because of the high point-cloud density, this standard deviation metric should reflect terrain variability and not vegetation cover. This measure serves as a DEM uncertainty and is highly spatially heterogeneous. Elevation and standard deviation maps for additional grid resolutions can be found in the Supplement (Supplemental Figures ~~14-16~~22-24). An island-wide canopy-height model can be found in Supplemental Figure ~~13-12~~.

## 6.3 Mapping Uncertainty on SCI

Using our standard deviation grids, we can then calculate both TE and PEU on SCI (see Supplemental Figure ~~17~~25). Using these two grids as inputs, we can also derive the QR across the entire SCI (Figure 10). Note that maximal QRs are low when compared to the theoretical models shown in Figures 6 and 8; this is due to both the much higher inherent noise in the real-world data, and to the more complex terrain represented by the lidar data.



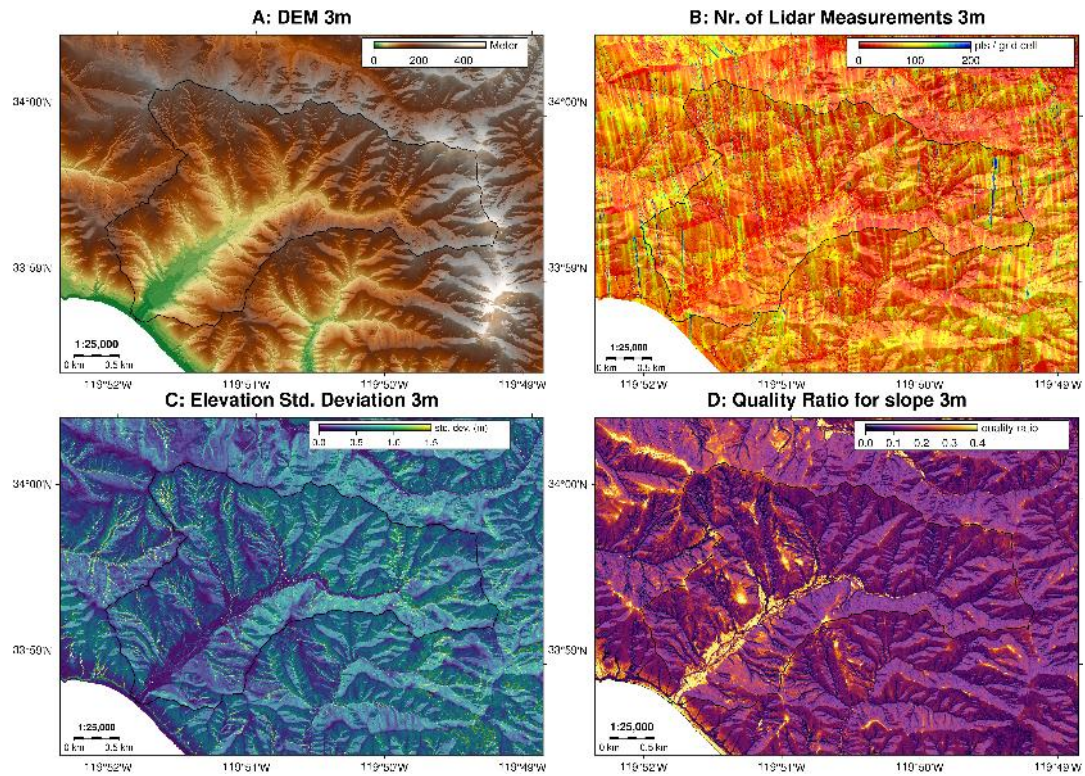


**Figure 10.** Selected metrics for the Pozo catchment in the southwestern part of SCI, calculated on the optimal grid resolution for this catchment (three meter grid). (A) Elevation, (B) lidar point density, (C) elevation standard deviation, (D) slope quality ratio (see Equation 14). The aspect quality ratio is shown in Supplemental Figure [18-26](#). A comparison of the elevation standard deviation and the lidar canopy height model is shown in Supplemental Figure [19-27](#).

#### 6.4 Identification of Optimal Grid Resolution

Using our pixel-wise standard deviations – and derived QRs – at each grid resolution, we can determine the island-wide optimal grid resolution for the calculation of topographic metrics which minimizes the combined influence of TE and PEU on our lidar dataset.

- 5 Unlike the synthetic data examined in Figure 6, the optimal grid resolution for aspect calculations is the same as that for slope. This is due to the distribution of both elevations and elevation uncertainties in the SCI DEM, and the different responses of slope and aspect calculations to the diverse terrain on SCI. Whole-island median TE, PEU, and QR can be found in Supplemental Table [1-2](#) for grid resolutions from one to ten meters. While four meters is the calculated optimal grid resolution, the QR peak is quite flat (see Figure 11), implying that both three-meter and five-meter DEMs will yield slope and aspect results of nearly
   
10 equal quality. Indeed, the TE and PEU magnitudes are similar for both metrics between three and five meters (see Supplemental Table [1-2](#)).

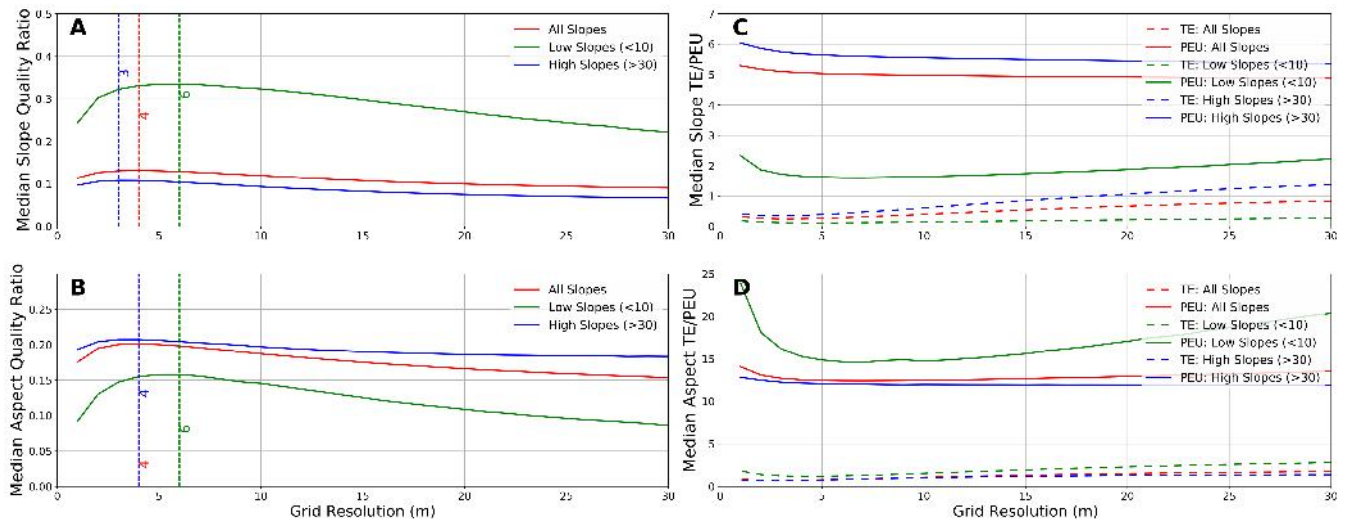


**Figure 11.** Median Quality Ratios (QRs) for all slopes, low slopes (<10) and high slopes (>30) across grid resolutions (1-30m). There is a clear trend where low slopes have better slope QRs, but worse aspect QRs. The optimal grid resolution for SCI is four meters for both slope and aspect. For inter-quartile ranges on the QRs, see Supplemental Figure 20-28.

It should be noted that a four-meter optimal grid resolution is likely too large for many applications, particularly those interested in micro-topography or other small-scale features. In those cases, [slope and aspect values calculated from a higher-resolution DEM](#) should be used with caution – PEU will continue to grow as grid resolution increases, and the rate of that increase will accelerate (see Figure 5). This effect will occur even if the DEM uncertainty decreases at smaller scales simply due to the larger impacts of PEU at very high grid resolutions. This means that the uncertainty bounds on slope and aspect estimates on very high resolution DEMs will increase quickly, which may limit some analyses. It is important to examine whether the data are precise enough to effectively resolve the features of interest. For high-resolution analyses, very high quality DEMs are required.

In this analysis of the airborne lidar dataset from SCI, we find that a four-meter DEM resolution minimizes the combined influence of TE and PEU. Slope and aspect analyses performed at this grid resolution have the smallest error bounds, and thus provide the most reliable data for analysis of topographic metrics over the entire island. [However, there exist other methods of choosing an appropriate DEM resolution for a given analysis, for example that of Roering et al. \(2010\).](#) We do not argue that our method is the best for all applications, but that our optimal grid resolution provides the smallest uncertainty for slope and aspect calculations over the entire dataset.

While a single, whole-island, grid resolution is useful in some applications, it is clear from Figure 10 that there are large spatial variations in the DEM uncertainty and the resulting QR, and hence in the optimal grid resolution. We can extend our method of identifying the optimal grid resolution on a catchment-by-catchment basis (Figure 12, map view in Supplemental Figure 24-29).

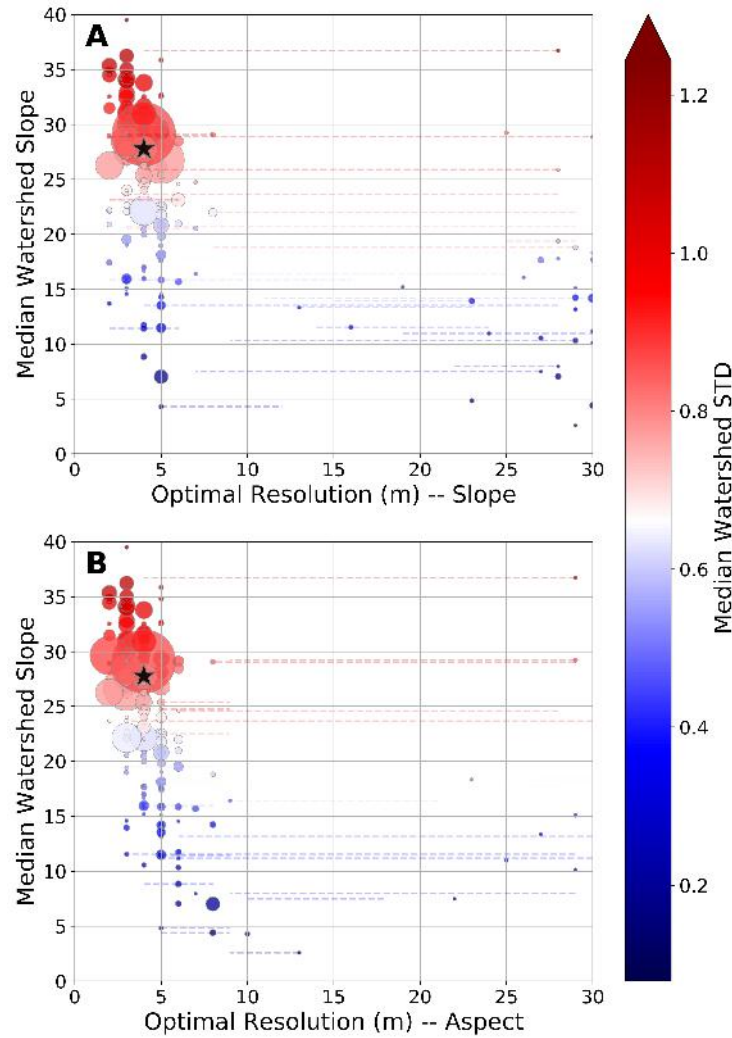


**Figure 12.** Optimal grid resolution for minimizing error bounds on slope and aspect calculations across SCI compared to catchment median slope. Point sizes are scaled to catchment size, from 0.1 to 34 km<sup>2</sup>. Dashed lines show the 25th percentile to 75th percentile of optimal grid resolution, colored by the standard deviation of that point. Stars show the whole-island optimal resolution and median slope. There exists a clear trend where lower median slopes lead to lower optimal grid resolutions. Standard deviations also tend to be smaller in these catchments, due to higher DEM fidelity over flat terrain. Catchments with low (>10 meter) optimal grid resolutions are small and have complex topography. For a map view of these results, we refer to Supplemental Figure [24-29](#).

There exist large spatial variations in the optimal grid resolution across SCI, driven by differences in terrain slope and DEM quality. When these differences are compared to median catchment slope and median catchment standard deviation, a clear pattern emerges (Figure 12). While there remains significant scatter in the data, catchments with high median slopes tend to

have both higher standard deviations and lower optimal grid resolutions. The data is bimodal, with the majority (83% for slope, 95% for aspect) of catchments having optimal resolutions below ten meters.

It is worth noting that the vast majority of the catchments with optimal slope and aspect resolutions above ten meters are small catchments concentrated on the northwestern edge of SCI (see Supplemental Figure 2129). These catchments have two unique topographic features which contribute to the high optimal grid sizes. (1) They have two distinct slope regimes: one steep hill of nearly constant slope, followed by one flatter residual marine terrace with a different constant slope. (2) The catchments drain into steep, deeply incised, cliffs. Interestingly, neither removing the steep cliffs (which have high elevation uncertainty), nor aggregating several small catchments into one larger analysis unit (to improve the statistical reliability of the median QR) result in higher optimal grid resolutions. We posit that the low optimal grid resolutions are a product of the unique two-stage topography in this region. However, an in-depth analysis of the specific factors which drive the optimal terrain resolution in each individual zone is outside of the scope of this manuscript. ~~In applying this~~

As a final application, we clipped out only the river networks on SCI to test whether they had higher or lower optimal grid resolutions than the island as a whole, or their individual catchments. We found that river networks, particularly those parts of the network which are in steep terrain, have higher elevation uncertainties, which leads to predicted higher optimal grid resolutions than the surrounding terrain. In applying our method of deriving optimal grid resolution, it is important to take into account the possibility of large differences in the optimal grid resolution over relatively small spatial scales, and to account for the differences in elevation uncertainty in different terrain types.

## 6.5 Island-Wide Slope and Aspect Distributions

As has been shown in Figures 6 and 11, there is clearly an optimal spatial resolution for the calculation of slope and aspect on our SCI lidar dataset. Furthermore, in Figure 8, it was shown that changes in QR can have a substantial impact on the slope and aspect distributions of a synthetic surface. This analysis can be extended to the SCI lidar data at a range of spatial scales (Figure 13).

There are clear differences in the slope and aspect distributions with increasingly poor QRs. This effect can also be seen in quantile-quantile plots of the entire SCI slope distribution when compared to the optimal grid resolution (see Figure 13C). Grid resolutions higher than the optimal result in slope distributions that are dominated by higher slopes, while lower resolutions tend towards lower slopes. This effect can be seen even when the grid resolution is only slightly removed from the optimal resolution (Supplemental Figure 2230). Notably, grid resolutions close to the optimal (e.g., three meters and five meters), have QRs and slope distributions that are very similar to the optimal four meter distribution.

As a final test of grid-resolution dependence, we resampled several grids to nominally match the optimal grid resolution – in this case we chose three meters for the Pozo catchment (see Figure 9, Supplemental Figure 2331) as the reference distribution. As can be seen in Figure 14A, there are differences between test (one to five meter) resolutions and the reference three meter histogram. When the test datasets are resampled to the three meter reference resolution using bilinear resampling (Figure 14B) and nearest neighbor resampling (Figure 14C), the histograms generally do not converge to the reference three meter distribution. The exception to this is when the one-meter data are resampled with a nearest neighbor approach, they converge



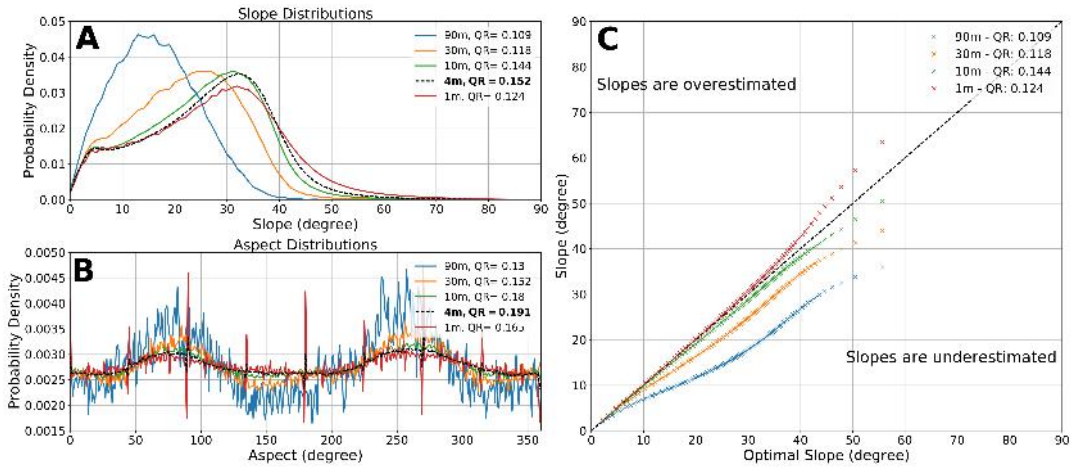


**Figure 13.** (A) Slope and (B) aspect differences across SCI DEMs, with QR calculated using SCI DEM elevation standard deviations (see Figure 10 and Supplemental Figures 13-15, 22-24). Optimal slope and aspect distributions plotted in black. (C) Quantile-quantile plot showing difference between the entire SCI slope distribution vs the ‘optimal’ (four meter) resolution. We observe a clear pattern in slope distributions where resolutions below the optimal resolution tend to overestimate slope, those below tend to underestimate slope.

to the three meter distribution. We attribute this effect to the lidar-gridding method – the three-meter data is drawn from the same neighborhood as the nine one-meter neighborhoods which are used for the one-meter gridding.

In general, slope distributions from resampled data should be used with caution; simply resampling elevation data to the optimal grid resolution before calculating slope does not guarantee better results – the DEM has to be created from the ungridded  
5 point data to fully take advantage of optimal gridding for slope calculations.

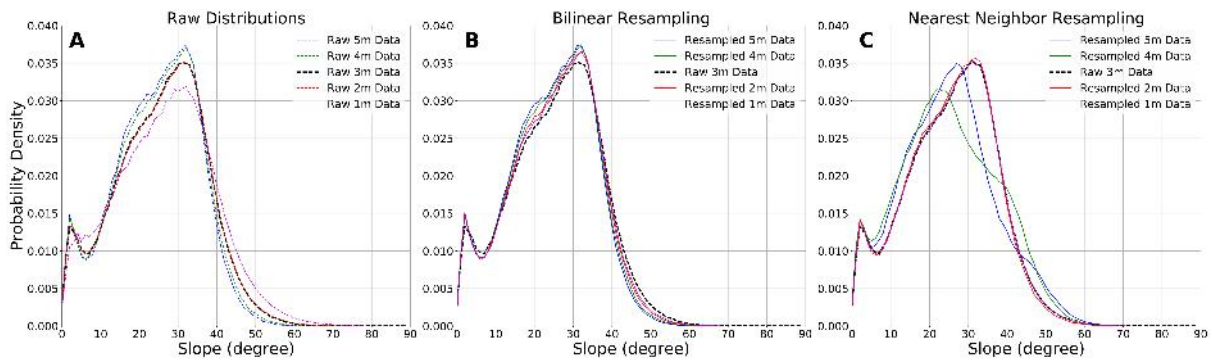


**Figure 14.** (A) Divergence of higher and lower grid-resolution slope distributions from that at the optimal resolution for the Pozo catchment (see Figure 9). Excepting the one meter histogram, the differences between resolutions are small. Right panels show slope distributions taken from one, two, four, and five meter data resampled to three meter resolution using (B) bilinear resampling and (C) nearest neighbor resampling. The resampled data distributions do not converge on the reference three meter distribution, excepting the one-meter data resampled with a nearest neighbor approach.

## 7 Conclusions

This study presents a detailed accounting of uncertainties and errors in the topographic metrics slope and aspect derived from both truncation errors and uncertainty in the underlying source digital elevation model (DEM). We first develop our analysis on synthetic data, which acts as a control dataset. We then extend our methodology onto a high point-density lidar dataset, which allows us to compare the relative impacts of gridding truncation errors and propagated elevation uncertainty on the calculation of topographic metrics.

From the analysis of both synthetic and real-world data, we identify the following key points: (1) the relative impact of truncation error and propagated elevation uncertainty can be captured in a single **quality**-metric, which we coin the Quality Ratio. This metric can be used to compare the accuracy of topographic metrics across DEM spatial resolutions and uncertainty distributions. (2) There exists an optimal grid resolution at which to calculate the topographic metrics slope and aspect for a given dataset that minimizes the total impact of both truncation error and propagated elevation uncertainty; the distribution of DEM uncertainties leads to spatial variation in the optimal grid resolutions at which to calculate slope and aspect. For ~~the~~ Santa Cruz Island in southern California, we find an optimal grid resolution of four meters, with island-average slope (aspect) errors of  $0.25^\circ$  ( $0.75^\circ$ ) for truncation error, and  $5^\circ$  ( $12.5^\circ$ ) for propagated elevation uncertainty. (3) Topographic metrics calculated at sub-optimal grid resolutions will have potentially large errors in their slope and aspect distributions. Resampling grids to the optimal resolution does not completely ameliorate these issues; it is important to generate the DEM at the optimal resolution from the underlying lidar dataset. (4) Slope and aspect calculations at high DEM resolutions ( $<3$  meters) are significantly impacted by the nonlinear relationship between grid spacing and propagated elevation uncertainty. A DEM with very low uncertainties is required to support robust analysis of fine-scale topography.

Given that grid-resolution-driven effects on regional slope and aspect distributions could have significant impacts on the interpretation of landscape morphology, we recommend that region-specific optimal DEM resolutions be determined before the calculation of topographic metrics.

*Code and data availability.* All codes and data for reproducing the results can be found in on GitHub (<https://github.com/UP-RS-ESP/TopoMetricUncertainty>).

*Author contributions.* T.S. led the development and writing of the MS, as well as the primary data analysis. A.R. contributed to the development of the methods and developed most of the python codes. B.B. contributed to the development of the methods and processed the lidar data.

*Competing interests.* The authors declare no competing financial interests.

*Acknowledgements.* The State of Brandenburg (Germany) through the Ministry of Science and Education and the NEXUS project supported T.S. for part of this study (grant to. B.B.). The authors thank Fiona Clubb and Ben Purinton for comments on an earlier version of the manuscript.

## References

- Abarbanel, S., Ditkowski, A., and Gustafsson, B.: On error bounds of finite difference approximations to partial differential equations—temporal behavior and rate of convergence, *Journal of Scientific Computing*, 15, 79–116, 2000.
- Ayalew, L. and Yamagishi, H.: The application of GIS-based logistic regression for landslide susceptibility mapping in the Kakuda-Yahiko Mountains, Central Japan, *Geomorphology*, 65, 15–31, 2005.
- 5 Baguskas, S. A., Peterson, S. H., Bookhagen, B., and Still, C. J.: Evaluating spatial patterns of drought-induced tree mortality in a coastal California pine forest, *Forest Ecology and Management*, 315, 43–53, 2014.
- Band, L. E.: Topographic partition of watersheds with digital elevation models, *Water resources research*, 22, 15–24, 1986.
- Bolstad, P. V. and Stowe, T.: An evaluation of DEM accuracy: elevation, slope, and aspect, *Photogrammetric Engineering & Remote Sensing*, 10 60, 7327–7332, 1994.
- Bookhagen, B. and Strecker, M. R.: Spatiotemporal trends in erosion rates across a pronounced rainfall gradient: Examples from the southern Central Andes, *Earth and Planetary Science Letters*, 327, 97–110, 2012.
- Carlisle, B. H.: Modelling the spatial distribution of DEM error, *Transactions in GIS*, 9, 521–540, 2005.
- Dibblee, T. W.: *Geologic Map of Western Santa Cruz Island*, Dibblee Geological Foundation, 2001.
- 15 Dietrich, W. E., Bellugi, D. G., Sklar, L. S., Stock, J. D., Heimsath, A. M., and Roering, J. J.: Geomorphic transport laws for predicting landscape form and dynamics, *Prediction in geomorphology*, 135, 103–132, 2003.
- Dunn, M. and Hickey, R.: The effect of slope algorithms on slope estimates within a GIS, *Cartography*, 27, 9–15, 1998.
- Durrán, D. R.: *Numerical methods for wave equations in geophysical fluid dynamics*, vol. 32, Springer Science & Business Media, 1999.
- Evans, I. S.: An integrated system of terrain analysis and slope mapping, *Zeitschrift für Geomorphologie*, 36, 274–295, 1980.
- 20 Farr, T. G., Rosen, P. A., Caro, E., Crippen, R., Duren, R., Hensley, S., Kobrick, M., Paller, M., Rodriguez, E., Roth, L., et al.: The shuttle radar topography mission, *Reviews of geophysics*, 45, 2007.
- Fisher, P. F.: Models of uncertainty in spatial data, *Geographical information systems*, 1, 191–205, 1999.
- Fisher, P. F. and Tate, N. J.: Causes and consequences of error in digital elevation models, *Progress in physical Geography*, 30, 467–489, 2006.
- 25 Florinsky, I. V.: Accuracy of local topographic variables derived from digital elevation models, *International Journal of Geographical Information Science*, 12, 47–62, 1998.
- Fornberg, B.: Generation of finite difference formulas on arbitrarily spaced grids, *Mathematics of computation*, 51, 699–706, 1988.
- Franklin, J.: Predictive vegetation mapping: geographic modelling of biospatial patterns in relation to environmental gradients, *Progress in physical geography*, 19, 474–499, 1995.
- 30 Grieve, S. W., Mudd, S. M., Milodowski, D. T., Clubb, F. J., and Furbish, D. J.: How does grid-resolution modulate the topographic expression of geomorphic processes?, *Earth Surface Dynamics*, 4, 627, 2016.
- Guisan, A. and Zimmermann, N. E.: Predictive habitat distribution models in ecology, *Ecological modelling*, 135, 147–186, 2000.
- Guzzetti, F., Carrara, A., Cardinali, M., and Reichenbach, P.: Landslide hazard evaluation: a review of current techniques and their application in a multi-scale study, Central Italy, *Geomorphology*, 31, 181–216, 1999.
- 35 Heuvelink, G. B., Burrough, P. A., and Stein, A.: Propagation of errors in spatial modelling with GIS, *International Journal of Geographical Information System*, 3, 303–322, 1989.



- Holmes, K., Chadwick, O., and Kyriakidis, P. C.: Error in a USGS 30-meter digital elevation model and its impact on terrain modeling, *Journal of Hydrology*, 233, 154–173, 2000.
- Hunter, G. J. and Goodchild, M. F.: Modeling the uncertainty of slope and aspect estimates derived from spatial databases, *Geographical Analysis*, 29, 35–49, 1997.
- 5 Kent, M.: *Vegetation description and data analysis: a practical approach*, John Wiley & Sons, 2011.
- Kirby, E. and Whipple, K. X.: Expression of active tectonics in erosional landscapes, *Journal of Structural Geology*, 44, 54–75, 2012.
- Kraus, K. and Pfeifer, N.: Determination of terrain models in wooded areas with airborne laser scanner data, *ISPRS Journal of Photogrammetry and remote Sensing*, 53, 193–203, 1998.
- Kyriakidis, P. C., Shortridge, A. M., and Goodchild, M. F.: Geostatistics for conflation and accuracy assessment of digital elevation models, *International Journal of Geographical Information Science*, 13, 677–707, 1999.
- 10 Lague, D.: The stream power river incision model: evidence, theory and beyond, *Earth Surface Processes and Landforms*, 39, 38–61, 2014.
- LAStools: Efficient LiDAR Processing Software (version 180831, academic), <http://rapidlasso.com/LAStools>, 2017.
- Lee, J., Fisher, P., Snyder, P., et al.: Modeling the effect of data errors on feature extraction from digital elevation models, *Photogrammetric Engineering and Remote Sensing*, 58, 1461–1461, 1992.
- 15 Montgomery, D. R. and Dietrich, W. E.: A physically based model for the topographic control on shallow landsliding, *Water resources research*, 30, 1153–1171, 1994.
- Mukul, M., Srivastava, V., Jade, S., and Mukul, M.: Uncertainties in the Shuttle Radar Topography Mission (SRTM) Heights: Insights from the Indian Himalaya and Peninsula, *Scientific Reports*, 7, 41 672, 2017.
- Neely, A., Bookhagen, B., and Burbank, D.: An automated knickzone selection algorithm (KZ-Picker) to analyze transient landscapes: Calibration and validation, *Journal of Geophysical Research: Earth Surface*, 122, 1236–1261, 2017.
- 20 Oksanen, J. and Sarjakoski, T.: Error propagation of DEM-based surface derivatives, *Computers & Geosciences*, 31, 1015–1027, 2005.
- Oksanen, J. and Sarjakoski, T.: Uncovering the statistical and spatial characteristics of fine toposcale DEM error, *International Journal of Geographical Information Science*, 20, 345–369, 2006.
- OpenTopography: 2010 channel islands lidar collection, <https://doi.org/10.5069/G95D8PS7>, 2012.
- 25 Ouma, Y. O. and Tateishi, R.: Urban flood vulnerability and risk mapping using integrated multi-parametric AHP and GIS: methodological overview and case study assessment, *Water*, 6, 1515–1545, 2014.
- Pelletier, J. D.: *Quantitative modeling of earth surface processes*, Cambridge University Press, 2008.
- Pelletier, J. D.: Minimizing the grid-resolution dependence of flow-routing algorithms for geomorphic applications, *Geomorphology*, 122, 91–98, 2010.
- 30 Pelletier, J. D.: A robust, two-parameter method for the extraction of drainage networks from high-resolution digital elevation models (DEMs): Evaluation using synthetic and real-world DEMs, *Water Resources Research*, 49, 75–89, 2013.
- Perroy, R. L., Bookhagen, B., Asner, G. P., and Chadwick, O. A.: Comparison of gully erosion estimates using airborne and ground-based LiDAR on Santa Cruz Island, California, *Geomorphology*, 118, 288–300, 2010.
- Perroy, R. L., Bookhagen, B., Chadwick, O. A., and Howarth, J. T.: Holocene and Anthropocene landscape change: arroyo formation on Santa Cruz Island, California, *Annals of the Association of American Geographers*, 102, 1229–1250, 2012.
- 35 Pierce, K. B., Lookingbill, T., and Urban, D.: A simple method for estimating potential relative radiation (PRR) for landscape-scale vegetation analysis, *Landscape Ecology*, 20, 137–147, 2005.

- Purinton, B. and Bookhagen, B.: Validation of digital elevation models (DEMs) and comparison of geomorphic metrics on the southern Central Andean Plateau., *Earth Surface Dynamics*, 5, 2017.
- Purinton, B. and Bookhagen, B.: Measuring Decadal Vertical Land-level Changes from SRTM-C (2000) and TanDEM-X (~ 2015) in the South-Central Andes, *Earth Surf. Dyn.*, 2018.
- 5 Rodriguez, E., Morris, C. S., and Belz, J. E.: A global assessment of the SRTM performance, *Photogrammetric Engineering & Remote Sensing*, 72, 249–260, 2006.
- Roering, J. J., Kirchner, J. W., and Dietrich, W. E.: Evidence for nonlinear, diffusive sediment transport on hillslopes and implications for landscape morphology, *Water Resources Research*, 35, 853–870, 1999.
- Roering, J. J., Marshall, J., Booth, A. M., Mort, M., and Jin, Q.: Evidence for biotic controls on topography and soil production, *Earth and Planetary Science Letters*, 298, 183–190, 2010.
- 10 Schmidt, J., Evans, I. S., and Brinkmann, J.: Comparison of polynomial models for land surface curvature calculation, *International Journal of Geographical Information Science*, 17, 797–814, 2003.
- Shortridge, A. and Messina, J.: Spatial structure and landscape associations of SRTM error, *Remote Sensing of Environment*, 115, 1576–1587, 2011.
- 15 Skidmore, A. K.: A comparison of techniques for calculating gradient and aspect from a gridded digital elevation model, *International Journal of Geographical Information System*, 3, 323–334, 1989.
- Smith, B. and Sandwell, D.: Accuracy and resolution of shuttle radar topography mission data, *Geophysical Research Letters*, 30, 2003.
- Snyder, N. P., Whipple, K. X., Tucker, G. E., and Merritts, D. J.: Landscape response to tectonic forcing: Digital elevation model analysis of stream profiles in the Mendocino triple junction region, northern California, *Geological Society of America Bulletin*, 112, 1250–1263, 2000.
- 20 Tarboton, D. G.: A new method for the determination of flow directions and upslope areas in grid digital elevation models, *Water resources research*, 33, 309–319, 1997.
- Thompson, J. A., Bell, J. C., and Butler, C. A.: Digital elevation model resolution: effects on terrain attribute calculation and quantitative soil-landscape modeling, *Geoderma*, 100, 67–89, 2001.
- 25 Tucker, G. E. and Bras, R. L.: Hillslope processes, drainage density, and landscape morphology, *Water Resources Research*, 34, 2751–2764, 1998.
- Tucker, G. E. and Hancock, G. R.: Modelling landscape evolution, *Earth Surface Processes and Landforms*, 35, 28–50, 2010.
- Wechsler, S.: Uncertainties associated with digital elevation models for hydrologic applications: a review, *Hydrology and Earth System Sciences*, 11, 1481–1500, 2007.
- 30 Wechsler, S. P. and Kroll, C. N.: Quantifying DEM uncertainty and its effect on topographic parameters, *Photogrammetric Engineering & Remote Sensing*, 72, 1081–1090, 2006.
- Wessel, B., Huber, M., Wohlfart, C., Marschalk, U., Kosmann, D., and Roth, A.: Accuracy assessment of the global TanDEM-X Digital Elevation Model with GPS data, *ISPRS Journal of Photogrammetry and Remote Sensing*, 139, 171–182, 2018.
- Whipple, K. X. and Tucker, G. E.: Dynamics of the stream-power river incision model: Implications for height limits of mountain ranges, landscape response timescales, and research needs, *Journal of Geophysical Research: Solid Earth*, 104, 17 661–17 674, 1999.
- 35 Zevenbergen, L. W. and Thorne, C. R.: Quantitative analysis of land surface topography, *Earth surface processes and landforms*, 12, 47–56, 1987.
- Zhang, J. and Goodchild, M. F.: Uncertainty in geographical information, CRC press, 2002.

- Zhang, W. and Montgomery, D. R.: Digital elevation model grid size, landscape representation, and hydrologic simulations, *Water resources research*, 30, 1019–1028, 1994.
- Zhou, Q. and Liu, X.: Error analysis on grid-based slope and aspect algorithms, *Photogrammetric Engineering & Remote Sensing*, 70, 957–962, 2004.